symmetry

MDPI

Review

Symmetry in Nuclear Physics and Astrophysics

Jelena Vesić

Jožef Stefan Institute, Jamova Cesta 39, 1000 Ljubljana, Slovenia; jelena.vesic@ijs.si

Abstract

Symmetry is a key principle in physics that links basic invariances to the structure of matter and the evolution of the universe. In this review, we use symmetry as a unifying thread connecting nuclear structure, nuclear reactions, and dense matter, and we highlight how symmetry-based arguments connect laboratory observables to astrophysical constraints. We present the essential concepts in a form accessible to a broad physics audience.

Keywords: nuclear symmetry; isospin; symmetry energy; neutron stars; equation of state; heavy-ion collisions; charge-exchange reactions; electric dipole moments; neutrinoless double-beta decay

1. Introduction

1.1. Motivation and Organization

Symmetry offers a compact way to formulate the laws of nature and helps explain why systems that differ widely in scale can exhibit similar behavior. In this review, symmetry serves as an organizing principle linking finite nuclei, reaction observables, and dense-matter inference. Where constraints rely on calibrated correlations, we distinguish statistical uncertainties from model-class and calibration systematics. The review is organized as follows: Section 2 introduces symmetry concepts used in nuclear physics; Section 3 describes experimental methodologies and technical capabilities, along with the dominant sources of systematic uncertainty; Section 4 connects laboratory constraints to inferred nuclear-matter parameters and shows how these propagate to neutron-star observables; Section 5 highlights near-term opportunities and precision tests, including frontiers beyond the Standard Model; and Section 6 summarizes the main conclusions and outlook.

1.2. Continuous and Discrete Symmetries: Conservation Laws and Fundamental Tests

Nuclei are composed of protons and neutrons that interact primarily through the strong interaction, while electromagnetic and weak interactions play essential roles in nuclear structure, stability, and decay. As a result, nuclei display systematic regularities that can often be traced back to symmetry principles and their controlled breaking. Continuous space–time symmetries and the associated conservation laws (Noether's theorem) are built into nearly all descriptions of nuclear structure and reactions [1]. In particular, time-translation symmetry implies conservation of energy; space-translation symmetry implies conservation of linear momentum; and rotational symmetry implies conservation of angular momentum [1]. Discrete symmetries such as parity (P), charge conjugation (C), and time reversal (T) play a fundamental role [2]. Violations of these symmetries test the Standard Model and provide sensitive discovery channels for physics beyond it, including searches for lepton-number violation (e.g., $0\nu\beta\beta$ decay) and charged-lepton flavor violation. Parity violation in weak interactions was first proposed by Lee and Yang

Check for updates

Academic Editor: Vasilis K. Oikonomou

Received: 15 January 2026
Revised: 12 February 2026
Accepted: 20 February 2026
Published: 3 March 2026

https://doi.org/10.3390/sym18030441

and then confirmed experimentally by Wu et al. [3,4]. CP violation has also been observed in weak-interaction processes [2]. The CP violation present in the Standard Model appears insufficient to account for the observed matter–antimatter asymmetry of the universe, motivating ongoing searches for additional sources of CP violation [5–7]. Searches for permanent electric dipole moments are among the most sensitive low-energy probes of such CP-violating physics, within and beyond the Standard Model [8,9].

1.3. Approximate and Emergent Symmetries in Nuclei

Beyond these fundamental symmetries, nuclear physics is shaped by approximate and emergent symmetries that reflect properties of the nuclear force and correlated many-body dynamics. Isospin symmetry, an approximate SU(2) invariance, treats protons and neutrons as two states of a single nucleon with respect to the strong interaction [10,11]. Although it is broken by the Coulomb force and by small charge-dependent components of the nuclear interaction, isospin remains a central organizing principle for nuclear spectra and reactions [12,13]. In the strong-interaction limit, it underlies mirror symmetry and the systematics of isobaric analog states [13–15]. At the many-body level, group-theoretical classifications such as SU(3), which provides a compact description of quadrupole collectivity, and $\mathrm{Sp}(3,\mathbb{R})$, a symplectic extension that systematizes rotational–vibrational dynamics, offer useful frameworks (see Section 2). More broadly, emergent and approximate symmetries provide compact classifications of spectra and transitions, while controlled symmetry breaking encodes the detailed dynamics and correlations (Section 2). These symmetry-guided regularities also motivate a familiar qualitative picture: the nucleus behaves like a quantum droplet. When many nucleons move coherently, a few collective degrees of freedom, such as quadrupole deformation and pairing correlations, often shape what we observe. However, similar level schemes can arise from distinct mechanisms (e.g., static deformation, configuration mixing in the shell model, or shape coexistence), which motivates careful separation of symmetry-based classification from mechanism.

1.4. Symmetry Energy, Isovector Dynamics, and Multimessenger Connections

With these symmetry concepts in mind, we now introduce the symmetry-energy parameters that connect laboratory observables to neutron-rich matter and astrophysical inference. A particularly important link between nuclear physics and astrophysics is the nuclear symmetry energy $S(n)$. For baryon density n (often written as ρ in the literature, with $\rho_0 \equiv n_s$ at saturation) and isospin asymmetry $\delta \equiv (n_n - n_p)/n$, and assuming invariance under $n_n \leftrightarrow n_p$ (neglecting isospin-breaking terms), so that odd powers of δ are absent, the energy per particle may be expanded as $e(n,\delta) \approx e(n,0) + S(n)\delta^2 + \mathcal{O}(\delta^4)$, thereby defining $S(n)$ as the leading isovector coefficient of the nuclear equation of state (EoS). We adopt the standard notation [16,17]:

$$J = S(n_\mathrm{s}), \qquad L = 3n_\mathrm{s}\left.\frac{dS}{dn}\right|_{n=n_\mathrm{s}}, \qquad K_\mathrm{sym} = 9n_\mathrm{s}^2\left.\frac{d^2S}{dn^2}\right|_{n=n_\mathrm{s}}. \tag{1}$$

Here, n_s denotes the saturation density of symmetric nuclear matter (often denoted as n_0), $n_\mathrm{s} \simeq 0.16\ \mathrm{fm}^{-3}$. Near saturation density, J is relatively well constrained, whereas L remains less tightly constrained by laboratory and theoretical analyses; the inferred ranges depend on the adopted models, observables, and statistical methodology [17–23]. Quoted ranges are typically conditional on a chosen framework and calibration strategy (e.g., within a given energy-density functional family, within chiral effective field theory with a specified truncation and extrapolation domain, or under specific Bayesian prior choices). Accordingly, cross-study comparisons should separate statistical uncertainties from framework-dependent systematics tied to modeling assumptions and calibration data. At supra-saturation densities, the density dependence of the symmetry energy contributes to the pressure of neutron-rich matter and influences neutron-star radii, tidal deformabilities, and crust properties, while contributing, together with the isoscalar sector, to the pressure of cold β-equilibrated matter relevant for the maximum mass [22,24–26]. The maximum mass is primarily set by the pressure at high density, i.e., by the overall stiffness of the equation of state in the relevant density range. Gravitational-wave observations beginning with GW170817 [27] and subsequent equation-of-state analyses, together with Neutron star Interior Composition Explorer (NICER) pulse-profile modeling of individual millisecond pulsars, suggest radii of order $\sim$11–13 km for canonical-mass neutron stars, with credible intervals that remain model-conditional and can extend below or above this depending on the adopted data set and inference setup [28–30].

Complementary to the density dependence of the symmetry energy is the isovector momentum dependence of the mean field, often summarized by an in-medium neutron–proton effective-mass splitting, $m_n^* - m_p^*$, in neutron-rich matter. Because both the definition and empirical constraints are framework- and analysis-dependent, we treat $m_n^* - m_p^*$ here as a compact proxy and discuss its role in transport observables in Section 3 [31,32].

1.5. Experimental Landscape and Key Probes

Experimentally, a broad suite of facilities and probes now enables quantitative tests of symmetry ideas and their breaking mechanisms across the nuclear chart and in nuclear matter. Rare-isotope facilities (e.g., the Facility for Rare Isotope Beams (FRIB), the Radioactive Ion Beam Factory (RIBF), the GSI Helmholtzzentrum für Schwerionenforschung (GSI)/Facility for Antiproton and Ion Research (FAIR), and the Systéme de Production d'Ions Radioactifs en Ligne de 2e génération (SPIRAL2) at the Grand Accélérateur National d'Ions Lourds (GANIL)) increasingly probe nuclei at extreme neutron–proton asymmetry, where weak binding and coupling to the particle continuum can enhance sensitivity to symmetry-related effects. High-resolution charge-exchange reactions, especially modern $(^3\mathrm{He}, t)$ measurements, map Gamow–Teller strength distributions [33–36] (see Section 3 for representative resolutions and their impact on extracted Gamow–Teller strength). While these advances enhance the experimental input, quantitative symmetry constraints still depend on reaction modeling, the treatment of the continuum and correlations, and (for some observables) on reliably disentangling competing multipoles. Additional information comes from β-decay studies of exotic nuclei, including decay studies of highly charged ions in storage rings, which provide complementary constraints on spin–isospin response and isospin-symmetry systematics [37]. Parity-violating electron scattering (PVES) (Section 3) provides a probe of neutron densities and the isovector response that is relatively insensitive to strong-interaction modeling, with remaining theory inputs dominated by electroweak radiative corrections, Coulomb distortions, and experimental systematics [38]. For completeness, we also briefly comment on symmetry-linked observables in relativistic heavy-ion collisions, including aspects of chiral symmetry restoration and the associated quark–hadron transition, as well as searches for the Quantum Chromodynamics (QCD) critical end point [39–41]. We also briefly discuss azimuthal anisotropy (anisotropic flow) and spin polarization as contextual complements in Section 3, noting that quantitative extractions are typically transport- and modeling-dependent, with dominant sensitivities to the mean-field momentum dependence, in-medium cross sections, cluster production, and, at higher energies, pion and resonance potentials. Finally, precision mass spectrometry, laser spectroscopy, and modern γ-ray spectroscopy and tracking arrays provide inputs such as masses, charge radii, electromagnetic moments, and transition strengths that enable quantitative studies of isospin symmetry, its breaking, and the density dependence of the symmetry energy [42–45].

2. Types of Symmetries in Nuclear Physics

In nuclear physics, symmetry is best viewed as a hierarchy: some invariances are exact and define conserved quantum numbers, while many others are approximate or emergent and become useful only within restricted model spaces, resolution scales, or dynamical regimes. At the most basic level, it refers to properties that remain unchanged under specific transformations, such as rotations, translations in space or time, or the (approximate) exchange of protons and neutrons. These include exact space–time invariances and discrete symmetries of the underlying interactions, approximate internal symmetries such as isospin and chiral symmetry [46], emergent collective symmetries associated with rotational and vibrational motion, more specialized regularities including pseudospin and F-spin, and, finally, situations in which symmetries are broken at the mean-field level and restored through quantum correlations [47–49]. Because different symmetry limits control different observables, the way symmetries break (Coulomb, spin–orbit, pairing, and continuum coupling) is often as informative as the symmetry itself. Throughout this section, we emphasize a pragmatic distinction: which symmetry-motivated quantities are directly constrained by data, and which enter only through modeling assumptions when mapping observables onto the isovector EoS and, ultimately, astrophysical inference. For clarity, we group the main symmetry ideas into six interconnected classes/themes: fundamental space–time symmetries; collective and group-theoretical symmetries; isospin and related charge symmetries; specialized symmetry-related regularities that emerge in particular regions of the nuclear chart; chiral and QCD-inspired symmetries; and symmetry breaking and restoration. Each class contributes in a distinct way to the phenomenology of finite nuclei and infinite nuclear matter, but together they highlight the unifying role of symmetry concepts in nuclear physics. Discrete symmetries (P, T, and (in the underlying relativistic-field-theory context) combinations involving C) connect nuclear observables to fundamental tests; we return to their experimental manifestations (e.g., EDM and parity-violating observables) in Section 3 and in the corresponding applications. Figure 1 provides a schematic map of these symmetry classes and their links to representative observables discussed in this review. Table 1 summarizes this classification and highlights representative symmetry concepts, their physical origins, and a few key observables.

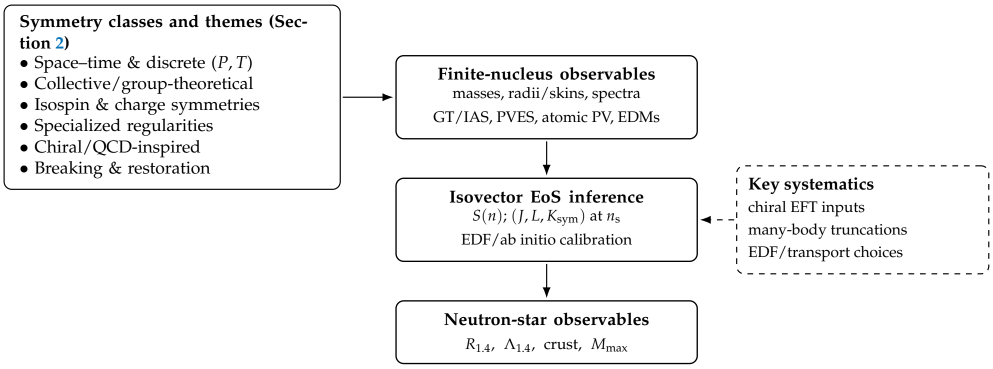

Figure 1. Overview linking symmetry classes (Section 2) to laboratory observables and, via isovector EoS inference, to neutron-star properties. The dashed arrow indicates model/analysis inputs that enter primarily at the EoS-inference stage. Abbreviations: P = parity; T = time reversal; GT = Gamow–Teller; IAS = isobaric analog state(s); PVES = parity-violating electron scattering; atomic PV = atomic parity violation; EDF = energy-density functional; EFT = effective field theory; n_s = saturation density; $R_{1.4}$ and $\Lambda_{1.4}$ denote the radius and tidal deformability of a $1.4\,M_\odot$ neutron star; M_{max} is the maximum gravitational mass; EDM = electric dipole moment.

Table 1. Symmetry classes and themes in nuclear physics and their physical roles (illustrative).

Class/Theme	Representative Symmetries	Physical Origin and Description	Key Phenomena and Observables
Fundamental space–time and discrete symmetries	Time translations; spatial translations; rotations; discrete P, T (and, in relativistic QFT, CPT)	Exact invariances tied to space–time structure for an isolated system; discrete-symmetry conservation/violation depends on the interaction (with CPT invariance ensured in local Lorentz-invariant QFT under standard assumptions)	Conservation of energy, momentum, and angular momentum; parity- and time-reversal-violation tests (e.g., EDMs, parity-violating observables)
Isospin and charge symmetries	SU(2) isospin; charge independence; charge symmetry ($p \leftrightarrow n$)	Approximate internal symmetry of the strong interaction treating protons and neutrons as an isospin doublet; broken by Coulomb and charge-symmetry/charge-independence breaking terms	Isobaric analog states (IAS); charge-exchange reactions; superallowed and allowed β-decay; IMME systematics; probes of isospin breaking (MED, TED, CDE; isospin mixing)
Collective and group-theoretical symmetries	SU(3); Sp$(3, \mathbb{R})$	Emergent (often approximate) symmetries arising from correlated many-body motion	Rotational bands; vibrational spectra; collective modes (including giant resonances); quadrupole collectivity
Specialized symmetries	Pseudospin; F-spin; cluster (molecular/algebraic) symmetries; seniority/pairing	Approximate or emergent regularities in specific regions of the nuclear chart and/or within restricted model spaces	Near-degenerate single-particle doublets; mixed-symmetry states; seniority systematics and pairing gaps; isoscalar $T = 0$ pairing
Chiral and QCD-inspired symmetries	Approximate chiral symmetry; chiral EFT	Approximate chiral symmetry of QCD and its spontaneous breaking; basis for low-energy nuclear forces and currents	Long-range pion exchange; consistent nuclear forces and electroweak currents; uncertainty quantification in chiral EFT
Symmetry breaking and restoration	Mean-field breaking of rotational symmetry and particle-number global $U(1)$ symmetry; explicit isospin breaking (Coulomb)	Efficient approximations that break symmetries at the mean-field level, restored by quantum correlations (projection, configuration mixing)	Deformation; pairing condensates; projection methods; configuration mixing; restoration of good quantum numbers; shape coexistence

Abbreviations: IAS = isobaric analog state(s); IMME = isobaric multiplet mass equation; MED = mirror energy difference(s); TED = triplet energy difference(s); CDE = Coulomb displacement energy; CSB = charge-symmetry breaking; CIB = charge-independence breaking; EDM = electric dipole moment; P = parity; T = time reversal; C = charge conjugation; CP = combined charge conjugation and parity; CPT = combined charge conjugation, parity, and time reversal; QFT = quantum field theory.

2.1. Fundamental Space–Time Symmetries

Space–time symmetries describe invariance under time translations, spatial translations, and rotations. These continuous symmetries underlie the familiar conservation laws of energy, linear momentum, and angular momentum [1]. Discrete symmetries such as parity (P) and time reversal (T) are more subtle in nuclear observables because their apparent conservation depends on the interaction that mediates the process (strong/EM interaction versus weak interaction). Charge conjugation (C) is not naturally defined as a symmetry operation for a fixed-A nucleonic many-body Hamiltonian (which does not include antiparticle degrees of freedom). It is most naturally discussed at the level of relativistic quantum field theory. In relativistic quantum field theory, CPT invariance is expected on very general grounds (under the usual assumptions of locality, Lorentz invariance, and unitarity) [50,51]. High-precision tests of CP, T, and CPT symmetries therefore provide sensitive low-energy tests of new physics [2,7–9]. In nuclei and atoms, these searches connect to concrete observables, including EDM experiments (probing CP/T violation) and parity-violating asymmetries.

2.2. Collective Symmetries

Collective symmetries emerge from correlated many-nucleon dynamics and offer compact descriptions of rotational and vibrational modes in light and medium-mass nuclei. A classic example is the (approximate) Elliott SU(3) symmetry of the harmonic-oscillator shell model, which organizes quadrupole collectivity and rotational-band structures. SU(3) provides a group-theoretical mapping between quadrupole deformation and rotational collectivity (its irreducible representations map onto intrinsic shapes and band structures). Although spin–orbit splittings and other non-harmonic terms break this symmetry in real nuclei, it often remains a useful classification scheme [52–55]. Symplectic extensions such as $\mathrm{Sp}(3,\mathbb{R})$ extend this idea to large-amplitude collective motion, multi-$\hbar\omega$ correlations, and deformation within a microscopic many-body description [54,55]. Here, $\mathrm{Sp}(3,\mathbb{R})$ (the real symplectic group) augments SU(3) by incorporating collective coordinate–momentum generators, enabling a unified microscopic description of coupled rotations and vibrations across major shells. Collective excitations such as giant resonances provide benchmarks of nuclear response and effective interactions in both the isoscalar and isovector channels [56,57].

2.3. Isospin Symmetry and Charge Symmetry

Isospin symmetry, introduced by Heisenberg and Wigner, treats protons and neutrons as two quantum states (often described as projections) of a single nucleon, forming an isospin doublet [10,11]. If this symmetry were exact for the strong interaction (i.e., neglecting electromagnetic effects and other isospin-nonconserving terms), nuclear interactions would be charge independent, and mirror nuclei would be identical in the strong-interaction limit. Coulomb shifts break this degeneracy [12]. In that strong-interaction limit, the members of an isobaric multiplet with the same A and total isospin T (i.e., different T_z) would be degenerate, providing a clean reference point for quantifying isospin breaking. Isospin symmetry is only approximate, but it captures essential features of the nuclear force and allows controlled deviations from it to be quantified. Accordingly, it provides a sensitive probe of Coulomb effects and charge-dependent components of the strong interaction [12,58]. Two related invariances commonly used to classify isospin-breaking effects are charge independence and charge symmetry. Charge independence refers to invariance under arbitrary rotations in isospin space, whereas charge symmetry refers specifically to invariance under a 180° rotation that exchanges protons and neutrons [12]. Charge-symmetry-breaking and charge-independence-breaking effects are observed in scattering-length differences, mirror energy shifts, non-degenerate isobaric analog states, and mirror asymmetries in β-decay [12,13,59]. High-precision mass measurements and systematics of isobaric analog states quantify these effects [14], and they serve as benchmarks for modern chiral effective field-theory interactions and energy-density functionals [46,60]. In practice, isospin-breaking systematics are often summarized through Coulomb displacement energies (CDE), mirror energy differences (MED), and (where applicable) triplet energy differences (TED), alongside isospin-mixing indicators.

Coulomb repulsion among protons breaks isospin symmetry and generates measurable phenomena such as Coulomb displacement energies, Thomas–Ehrman shifts in weakly bound nuclei, and enhanced isospin mixing near the proton drip line [13,58,61–63]. Experi-

https://doi.org/10.3390/sym18030441

ments on proton-rich exotic nuclei reveal pronounced asymmetries in decay and transition strengths close to the drip line, where small separation energies enhance sensitivity to Coulomb effects and coupling to the continuum [64]. β-decay spectroscopy of ^{27}S provides a representative recent experimental example [59]. Mirror nuclei serve as probes of the charge-dependent nuclear interaction [12,63]. A particularly sensitive class of observables is provided by mirror energy differences (MED) between analog states in $T = 1/2$ nuclei. A systematic shell-model analysis of MED in the $A = 42$–54 region has been used to constrain effective isovector interactions $(V_{pp} - V_{nn})$ that include both Coulomb and nuclear charge-dependent terms [13,63]. The results indicate that Coulomb effects alone do not reproduce the full MED systematics and that additional isospin-nonconserving nuclear contributions are required in effective Hamiltonians [63]. Such studies therefore place constraints on charge-symmetry-breaking and charge-independence-breaking terms in modern shell-model descriptions.

2.4. Pseudospin, F-Spin, and Other Specialized Symmetries

Some nuclear symmetries are more abstract and can be viewed as regularities in the single-particle spectrum or in patterns of collective states. In practice, these symmetries serve as a guide to near-degeneracies and selection-rule systematics even when the underlying dynamics are complex. Pseudospin and F-spin are examples of such “internal” symmetries: pseudospin helps organize single-particle levels into near-degenerate doublets [65,66], while F-spin provides a useful classification of proton–neutron degrees of freedom in collective models [47,48]. These ideas are particularly useful in heavy nuclei and along isotopic chains, where regularities emerge despite complex spectra. In relativistic mean-field language, pseudospin symmetry emerges as an approximate symmetry when the sum of the Dirac scalar and vector mean fields, $\Sigma(r) \equiv V_S(r) + V_V(r)$, is approximately constant (or slowly varying) over the radial domain relevant for the single-particle wave functions (i.e., $d\Sigma/dr \approx 0$ in the pseudospin-symmetric limit), which reflects an underlying SU(2) symmetry of the Dirac Hamiltonian [65,66]. In typical relativistic mean-field potentials, this pseudospin limit is associated with a partial cancellation between V_S and V_V over the relevant radial domain, so pseudospin doublets become only approximately (not exactly) degenerate. This pseudospin perspective clarifies the relativistic origin of shell structure and its evolution toward weakly bound systems. Furthermore, F-spin symmetry within the proton–neutron interacting boson model (IBM-2) [47,48] provides a systematic way to classify proton and neutron bosons, in which the F-spin quantum number F quantifies proton–neutron mixing. Mixed-symmetry states, typically associated with the F-spin sector $F = F_{\max} - 1$ in the IBM-2 classification, serve as sensitive probes of proton–neutron correlations and of the evolution of collective behavior along isotopic chains (see, e.g., [67–69]). Near the drip lines, where nuclear binding is weak, halo nuclei such as ^{11}Li and ^{6}He display extended matter distributions, altered pairing correlations due to continuum coupling, and enhanced low-energy electric dipole (E1) strength [70]. Cluster configurations, including α clustering in ^{12}C and ^{16}O, reveal emergent spatial symmetries and are effectively modeled using algebraic and microscopic cluster theories [71]. Shape coexistence, defined by the presence of multiple nuclear shapes at comparable energies, indicates the existence of competing local minima in the nuclear energy landscape and can be analyzed through configuration mixing and mean-field-based studies [72]. Unconventional pairing correlations are expected to be most pronounced in $N \approx Z$ nuclei in the mass $A \approx 90$–100 region, where neutrons and protons occupy the same high-j orbitals and isovector ($T = 1$) and isoscalar ($T = 0$) correlations may compete [73]. Evidence that has been interpreted as consistent with a spin-aligned $T = 0$ pairing phase has been reported in the $N = Z = 46$ nucleus ^{92}Pd, where the yrast level pattern was interpreted in terms of spin-aligned neutron–proton (np) pairs [74]. This behavior differs from the level schemes of neighboring nuclei and suggests that approximate symmetries in the pairing channel may evolve qualitatively toward the $N = Z$ line. Pairing correlations can also be discussed in terms of an approximate seniority symmetry, which classifies states by the number of unpaired nucleons and explains level systematics near shell closures [75].

2.5. Chiral Symmetry and QCD-Inspired Symmetries

At the most fundamental level, nuclear structure and interactions emerge from Quantum Chromodynamics (QCD) [76]. While QCD cannot yet be solved routinely for complex nuclei, its approximate chiral symmetry provides the symmetry basis for constructing the low-energy nuclear force within effective field theory [46,77–79]. The spontaneous breaking of chiral symmetry in the QCD vacuum gives rise to pions as pseudo-Goldstone bosons; consequently, pion exchange governs the long-range part of the nuclear interaction and provides a leading contribution to its characteristic spin–isospin dependence [46,79]. (Chiral symmetry is also explicitly broken by the light-quark masses, which is reflected in the finite pion mass.) At high temperature and/or baryon density, chiral symmetry is expected to be (approximately) restored; its interplay with the quark–hadron transition (and possible QCD critical end point) motivates dedicated experimental and theoretical studies in relativistic heavy-ion collisions [39,40]. A brief phenomenological discussion of these high-temperature symmetry aspects and their representative observables is deferred to Section 3. Chiral effective field theory (chiral EFT), a low-energy implementation of QCD symmetries, incorporates these symmetry constraints and provides a systematic expansion of nuclear forces and currents, including consistent many-body interactions, together with a framework for estimating truncation uncertainties [46,76,79].

Quantitative predictions and uncertainty budgets remain sensitive to regulator choices, the calibration of low-energy constants (LECs), and assumptions about the breakdown scale of the expansion [76,79]. Within this framework, pion exchange and associated two-body axial currents provide important contributions to GT transitions, β-decay, and neutrino–nucleus scattering [76,80]. Recent ab initio calculations based on chiral EFT interactions have clarified links between the properties of finite nuclei, neutron matter, and the nuclear symmetry energy, enabling constraints to be propagated within model-conditional calibration and density-extrapolation strategies to astrophysical observables such as neutron-star radii and tidal deformabilities [19,20].

2.6. Symmetry Breaking and Restoration in Nuclei

Mean-field descriptions of nuclei often involve intrinsic states that break symmetries of the underlying Hamiltonian [81]. Typical examples include the breaking of rotational symmetry in deformed nuclei and particle-number symmetry in pairing condensates, as well as explicit isospin breaking by the Coulomb interaction. This intrinsic (spontaneous) symmetry breaking is not an exact property of the physical system; rather, it reflects an efficient approximation to the correlated many-body state. Equivalently, broken-symmetry intrinsic states are convenient reference states. Good quantum numbers are recovered once correlations are incorporated through symmetry restoration (projection) and, where necessary, configuration mixing. Typically, symmetry restoration is implemented by combining projection techniques with configuration mixing frameworks such as the generator-coordinate method (GCM) [81]. Angular-momentum projection yields states with good rotational quantum numbers and generates rotational band structures, while particle-number projection improves the description of pairing correlations. Collective symplectic structures may re-emerge even when SU(3)-like symmetries are strongly broken at the single-particle level [54,55]. The interplay between symmetry breaking and restoration provides a measure of many-body correlations and is needed for reliable descriptions of spectra and transition strengths. With this taxonomy in place, we now turn to the experimental methodologies that most directly access these symmetry concepts and quantify their breaking mechanisms (Section 3).

3. Experimental Methodologies and Technical Capabilities

Nuclear symmetry studies rely on multiple, mutually constraining experimental approaches that probe complementary aspects of nuclear structure, dynamics, and interactions in neutron–proton-asymmetric systems. They combine probes that constrain different parameter combinations (e.g., neutron densities and isovector response in finite nuclei, spin–isospin strength via charge-exchange and decay, and symmetry-energy sensitivity in transport observables), so that inference is driven by cross-consistency rather than any single observable. No single measurement uniquely fixes all symmetry-relevant quantities, and robust constraints therefore require joint analyses that propagate both experimental and model uncertainties. Accordingly, quantitative inferences typically combine several observables, propagate theoretical and experimental uncertainties, and leverage modern accelerator and detector capabilities. We focus on experimental observables that most directly enter symmetry-energy and isovector EoS constraints, and we highlight, case by case, the dominant interpretation systematics (reaction theory, detector response, and model dependence of the mapping from measured quantities to $S(n)$ or (for astrophysical applications) to the pressure $P(n)$ of cold neutron-rich matter at density n). For each method, we highlight specific symmetry aspects, such as the density dependence of the symmetry energy, isospin-symmetry breaking, or the spin–isospin response, and where relevant indicate how laboratory observables can be connected, directly or indirectly, to neutron-star (and, more conditionally, supernova) physics [21,33,82–84].

3.1. Heavy-Ion Collisions and the Symmetry Energy

Heavy-ion collisions probe the symmetry energy over a broad range of densities and temperatures, but quantitative constraints depend on transport simulations and their associated modeling systematics [82,83,85]. The isovector mean field associated with the symmetry energy provides the restoring force that drives neutron–proton separation, equilibration, and emission (and corresponds, in uniform matter, to an isovector contribution to the pressure) [82,83]. At finite temperature and out of β equilibrium, heavy-ion data constrain an effective isovector EoS; the mapping to $S(n)$ (and to (J, L, K_{sym})) is therefore analysis-conditional and should be stated explicitly. At near-Fermi energies (roughly 30–100 MeV per nucleon), collisions undergo compression–expansion dynamics that predominantly sample sub-saturation to near-saturation densities [82,83]. Key observables include isospin diffusion, isoscaling parameters extracted from fragment yields [86], and neutron-to-proton spectral ratios, reflecting both mean-field dynamics and transport properties [82,83,87]. Constraints are obtained by confronting transport calculations with ensembles of isospin-sensitive observables rather than by inverting any one measurement in isolation. As noted in Section 1, the resulting bands are therefore model- and analysis-conditional and should be interpreted together with the transport inputs and calibration strategy. Within transport-model analyses, the inferred degree of isospin equilibration can shift systematically with the assumed sub-saturation isovector stiffness, thereby informing constraints on the slope parameter L within a chosen parameterization (often at fixed J) when combined with systematic uncertainty estimates. At the same time, these observables also respond to other transport inputs; examples of dominant uncertainty drivers include the momentum dependence of the mean field, in-medium nucleon–nucleon cross sections, cluster production and coalescence prescriptions, and (at higher energies) pion production/absorption dynamics and pion/kaon optical potentials. Quantitative results should therefore be reported as code- and observable-specific bands with clearly stated assumptions (see also Section 4) [21,87,88]. A central limitation is parameter degeneracy: similar trends can arise from the isovector mean field, in-medium cross sections, cluster production, and event selection, and the inferred symmetry-energy sensitivity can vary across transport implementations [89,90]. A further entangled isovector ingredient is the momentum dependence of the mean field, commonly parameterized in terms of an in-medium neutron–proton effective-mass splitting, $m_n^* - m_p^*$, in the transport-model (momentum-dependent mean-field/Landau-mass) sense. Because m^* governs the energy and momentum dependence of single-particle propagation and emission, isospin-sensitive observables (e.g., neutron/proton spectral ratios, differential flows, and meson-production systematics) can respond to $m_n^* - m_p^*$ in addition to $S(n)$. Accordingly, symmetry-energy constraints extracted from heavy-ion data are conditional on assumptions about the isovector momentum dependence; robust transport inferences should therefore report—or marginalize over—the adopted $m_n^* - m_p^*$ behavior alongside the symmetry-energy parameterization within a given framework [82,83,88,89]. At higher beam energies (roughly 400 MeV/A to $\sim$2–3 GeV/A), experiments access supra-saturation densities using meson and photon observables, most prominently pion and kaon production ratios [91,92]. Ratios such as π^-/π^+ increase with neutron excess and, in some transport-model implementations, have been linked to a softer symmetry energy at high density, though the sign and magnitude of the sensitivity can change across implementations, and the interpretation remains strongly model-dependent [91,93]. The inferred high-density behavior shifts when Δ dynamics, pion production/absorption, and meson potentials are treated differently. Accordingly, pion-based constraints are conditional on the transport implementation [90,93]. Kaon ratios (K^0/K^+) have been proposed as complementary probes that can be less sensitive to some late-stage hadronic effects in certain regimes, while remaining sensitive to in-medium kaon potentials and the underlying mean field [94]. Hard photons from neutron–proton bremsstrahlung are emitted mainly in the early, pre-equilibrium stage and, because they have comparatively little final-state interaction, provide a penetrating probe of the reaction dynamics [95]. Quantitative inferences at supra-saturation density can vary significantly across transport implementations due to differences in mean fields, cluster production, in-medium cross sections, and meson potentials. Results should be reported with explicit code dependence and prior sensitivity, ideally guided by inter-code benchmarks [89]. For the mapping from these reaction observables to symmetry-energy parameters and neutron-star implications, we refer to Section 4. In addition to symmetry-energy-sensitive observables, relativistic heavy-ion collisions provide symmetry-linked probes that are often framed explicitly in symmetry language. Anisotropic flow coefficients v_n quantify the breaking of azimuthal symmetry by the initial geometry and its hydrodynamic/transport response [96], while global and local spin polarization quantify a breaking of up–down symmetry in the produced matter [97]. At sufficiently high temperature and/or baryon density, these collisions also provide access to aspects of chiral symmetry restoration and the quark–hadron transition (including possible critical-point searches); quantitative extractions in this domain are typically conditional on the adopted initial-state modeling, transport/hydrodynamic evolution, and hadronization prescriptions [39–41]. Key experimental efforts include the ASY-EoS campaign at GSI [98] and large-acceptance spectrometer systems such as SAMURAI (Superconducting Analyzer for MUlti-particles from RAdio Isotope beams) at the RIKEN Radioactive Isotope Beam Factory (RIBF) [99] and LAMPS (Large Acceptance Multi-Purpose Spectrometer) at RAON (Rare isotope Accelerator complex for ON-line experiments) [100], which combine high-granularity tracking with charged-particle and neutron detection to improve the interpretability of isospin-sensitive observables.

3.2. Charge-Exchange Reactions and Spin-Isospin Probes

Charge-exchange reactions, such as (p,n), (n,p), (d,^{2}He), and (^{3}He,t), provide a selective probe of the nuclear spin–isospin response by accessing $\Delta T_z = \pm 1$ transitions that are the hadronic analogs of weak processes [101–103]. In particular, Gamow–Teller transitions ($\Delta L = 0$, $\Delta S = 1$, $\Delta T = 1$) dominate many allowed β-decay channels and are central to weak rates in stars [33,104]. At intermediate energies and forward angles, the approximate proportionality between GT strength and the charge-exchange cross section at small momentum transfer provides an empirical pathway to reconstruct GT distributions and assess quenching and configuration mixing [101–103]. From an experimental perspective, modern charge-exchange campaigns rely on high-resolution magnetic spectrometers and advanced focal-plane detection, often reaching $\sim$10–30 keV energy resolution in the forward-angle regime [34,105–107]. Inverse-kinematics charge exchange with radioactive beams is also developing rapidly, motivated by access to very neutron-rich systems and by the need to constrain the weak response far from stability; active targets and large-acceptance spectrometers are key enabling technologies [108–110].

Isobaric analog states (IAS), reached through Fermi transitions ($\Delta L = 0$, $\Delta S = 0$), provide a clean benchmark for isospin symmetry and its breaking and tightly constrain Coulomb/isospin-breaking systematics. Their interpretation remains conditional on the adopted structure and Coulomb-correction framework [13–15]. High-resolution (^{3}He,t) spectroscopy has enabled detailed studies of IAS fragmentation and isospin mixing in medium-mass systems [35]. Beyond extracting GT strengths relevant for β-decay, these data provide a stringent testbed for microscopic structure models and for reaction-theory systematics, with residual model dependence entering through optical potentials, effective interactions, and multi-step contributions [13,35].

3.3. β-Decay and Weak-Interaction Observables

β-decay provides a complementary window on weak-interaction couplings, isospin structure, and symmetry breaking, particularly in nuclei close to the drip lines where weak binding and coupling to the continuum can reshape wave functions and transition strengths [64,111]. It samples the vector and axial-vector weak currents through Fermi (isospin) and GT (spin–isospin) operators, thereby constraining nuclear matrix elements that also enter astrophysical weak rates [104]. Precision tests additionally require radiative and isospin-symmetry-breaking corrections [112]. In-flight projectile fragmentation (or ISOL (isotope separation on-line) production) followed by implantation into highly segmented double-sided silicon strip detectors (DSSSDs) enables event-by-event correlations between implanted ions and subsequent decays [113,114]. This approach supports the identification of very rare decay branches and the detection of low-energy charged particles, including β-delayed protons with energies down to the sub-MeV regime (and, in favorable cases, a few hundred keV), provided that thresholds, β summing, and correlation-window backgrounds are carefully controlled [111,113]. Such sensitivity is especially crucial near the proton drip line, where small proton separation energies enhance Coulomb and continuum effects and mirror asymmetries in β-decay can become pronounced; the β-decay spectroscopy of ^{27}S provides a representative example and attributes a large mirror asymmetry to weak-binding effects in the proton $1s_{1/2}$ orbit [59]. High-precision half-life and Q-value measurements, using Penning traps and dedicated decay stations (and, in selected cases, storage-ring techniques), are central to tests of the weak interaction and the unitarity of the Cabibbo–Kobayashi–Maskawa (CKM) matrix, most notably through superallowed $0^+ \to 0^+$ transitions. They require systematic control of radiative and isospin-symmetry-breaking corrections [112]. β-delayed particle emission (protons, neutrons, α particles) provides access to unbound states and resonance properties in exotic nuclei and remains one of the most direct experimental routes to spectroscopy at and beyond the drip lines. Quantitative interpretation can depend on line-shape modeling, detector response, and feeding from unresolved states [64,111]. Beyond single-particle emission, multi-particle decay modes (e.g., $\beta 2p$, $2p$, and correlated emissions) probe nucleon–nucleon correlations in weakly bound systems. Recent developments in highly segmented implantation arrays and tracking detectors improve reconstruction of complex decay topologies, but require careful efficiency calibration and event-classification systematics [64,114].

3.4. Gamma-Ray Spectroscopy and Lifetime Measurements

Gamma-ray spectroscopy provides experimental access to nuclear level schemes and electromagnetic decay patterns, enabling structural systematics that frequently expose emergent symmetries (e.g., rotational and vibrational sequences) and their breaking. High-efficiency Compton-suppressed HPGe (high-purity germanium) arrays such as GAMMASPHERE [115] and INGA (Indian National Gamma Array) [44,116] provide high photopeak efficiency and excellent energy resolution, while tracking arrays such as AGATA (Advanced GAmma Tracking Array) [45] and GRETINA (as the first stage toward the full 4π Gamma-Ray Energy Tracking Array (GRETA) concept) [117,118] enable interaction-position reconstruction for event-by-event Doppler correction and γ-ray tracking. The measured energies establish level spacings and band or multiplet structures. Intensities, angular distributions, and angular correlations constrain branching ratios, multipolarities, and mixing ratios, enabling quantitative comparisons with collective and shell-model descriptions. Lifetime measurements (using DSAM (Doppler-shift attenuation method), recoil-distance/plunger methods, and fast-timing techniques) set the absolute scale of transition strengths through $B(EL)$ and $B(ML)$ values. The recoil-distance Doppler-shift (RDDS) method provides access to lifetimes and absolute transition probabilities in the $\sim 10^{-12}$–10^{-9} s range over a broad range of reactions and kinematics [119], while modern γ–γ fast timing with LaBr$_3$(Ce) extends sensitivity to very short lifetimes with well-characterized timing response functions [120]. These observables constrain electromagnetic matrix elements and help disentangle isoscalar and isovector components. For example, in the $A = 31$ mirror pair, selected $E1$ strengths exhibit a sizable isoscalar admixture relative to the isovector component (reported at the $\sim$24% level) [121]. Systematic studies of proton–neutron mixed-symmetry excitations in vibrational and transitional nuclei provide stringent constraints on proton–neutron quadrupole correlations and on the effective interactions used in collective models [67]. A main practical challenge is that precision electromagnetic matrix elements are often limited by systematic effects rather than statistics: efficiency and summing corrections, Doppler-reconstruction systematics (velocity distributions, stopping powers, and lineshape modeling), side-feeding and unresolved feeding, angular-correlation assumptions, and the treatment of background and contaminant lines. Accordingly, robust conclusions about symmetry signatures usually require redundant observables (energies, branching ratios, mixing ratios, lifetimes) and cross-checks across reaction mechanisms and detector configurations [119,120].

3.5. Parity-Violating Electron Scattering

Parity-violating electron scattering exploits the weak neutral current to constrain neutron distributions and related isovector properties relevant to the symmetry energy. The parity-violating asymmetry arises from γ–Z^0 interference [122,123]. It is defined as

$$A_{\mathrm{PV}} = \frac{\sigma_R - \sigma_L}{\sigma_R + \sigma_L}, \tag{2}$$

where $\sigma_{R(L)}$ denotes the differential cross section for right- (left-) handed electrons. The neutron weak charge is much larger in magnitude than the proton weak charge [2,124]. As a result, $A_{\rm PV}$ is primarily sensitive to the nuclear weak form factor and thus to the neutron density, with substantially reduced strong-interaction reaction-model dependence compared to hadronic probes [125–127]. Quantitative extractions require treatment of Coulomb distortions, electroweak radiative corrections, acceptance averaging, and backgrounds, which are among the dominant sources of systematic uncertainty [125,127]. PVES isolates the weak neutral-current response at fixed momentum transfer, constraining the weak-charge form factor [122,123]. Translating $A_{\rm PV}$ into a neutron radius or skin requires a nuclear-structure parameterization and quantified theory input. Helicity-correlated instrumental effects and electroweak radiative corrections often set the scale of systematic uncertainties, while the total uncertainty in flagship measurements can still be partly statistics-limited after systematic controls are established in the final data set. Experiments such as PREX (Pb Radius Experiment) [125,126] and CREX (Ca Radius Experiment) [127] employ highly polarized electron beams, precision magnetic spectrometers, dedicated Cherenkov detectors, and ultra-stable helicity control and beam monitoring to measure extremely small asymmetries. For elastic scattering at PREX/CREX kinematics, the asymmetries are typically at the sub-ppm to a few ppm scale (i.e., $\mathcal{O}(10^2\text{–}10^3)$ ppb), e.g., $A_{\rm PV} \approx 5.5 \times 10^2$ ppb for ^{208}Pb and $A_{\rm PV} \approx 2.668 \times 10^3$ ppb for ^{48}Ca depending on the kinematics [126,127]. Related parity-violation measurements on the proton (Qweak) probe the weak charge of the proton at comparably small asymmetries [128]. PVES permits the extraction of neutron radii and neutron-skin thicknesses with reduced strong-interaction model dependence; connecting those radii to symmetry-energy parameters typically proceeds through correlations within calibrated nuclear energy-density functionals [17]. These measurements provide indirect constraints on the density dependence of the symmetry energy, commonly parameterized by the slope L [17]. PREX-II indicates a comparatively large neutron skin in ^{208}Pb [126], while CREX favors a smaller neutron skin in ^{48}Ca [127]. Achieving a consistent description across nuclei and momentum transfers has therefore become a key benchmark for EDF developments and uncertainty-quantified inferences [17,129]. The neutron-skin–to–L step is correlation-based within a chosen EDF calibration strategy (see Section 4 and Figure 2). PVES most directly constrains the weak form factor at the measured momentum transfer.

3.6. Radioactive Ion Beams and Exotic Nuclei

Modern radioactive-ion-beam (RIB) infrastructures, including in-flight fragmentation facilities, ISOL facilities, and storage-ring precision experiments, enable systematic studies of nuclei far from stability, where weak binding, continuum coupling, and large isospin asymmetry amplify symmetry breaking and emergent collective patterns. RIBs provide access to nuclei with extreme N/Z, allowing tests of nuclear interactions and many-body approximations in regimes that are inaccessible with stable beams. In-flight fragmentation and separation offer broad isotope coverage at intermediate and high energies, while ISOL techniques can deliver beams of high purity and excellent beam quality for precision experiments. Precision masses and selected spectroscopic observables can be extended to very short-lived nuclides using storage-ring techniques (including isochronous and Schottky mass spectrometry), reaching lifetimes from the tens-of-μs to ms regime in favorable conditions, depending on the mode and nuclei [130–134]. RIB experiments probe halo and skin phenomena, shell evolution, and isospin mixing in weakly bound systems through different reaction mechanisms. Coulomb excitation in inverse kinematics provides access to $E2$ and $E3$ matrix elements and hence to deformation, shape coexistence, and proton–neutron collectivity, including mixed-symmetry quadrupole modes [67,135,136]. Knockout, breakup, and charge-changing reactions, analyzed with eikonal/Glauber-based and continuum-sensitive descriptions, provide spectroscopic information and can constrain neutron-skin trends and symmetry-energy-related systematics when combined with theory [84,136]. Invariant-mass spectroscopy of unbound states in neutron-rich nuclei relies on large-acceptance spectrometers and high-efficiency neutron time-of-flight (ToF) arrays. Representative systems include LAND (Large Area Neutron Detector) at GSI and large-acceptance spectrometers SAMURAI at RIKEN, as well as MoNA–LISA (Modular Neutron Array–Large multi-Institutional Scintillator Array) at NSCL (National Superconducting Cyclotron Laboratory)/FRIB for multi-neutron detection [137–140]. Here, the dominant experimental uncertainties are crosstalk, efficiency calibration, and acceptance effects. On the theory side, continuum dynamics and final-state interactions can dominate the extracted resonance properties. Results should therefore be reported together with clearly stated reconstruction procedures, efficiency and cross-talk corrections, and sensitivity studies to the adopted reaction and continuum models [138].

3.7. Precision Mass Measurements and Isospin Structure

Nuclear masses provide binding energies and their finite differences (separation energies and Q values), and therefore yield direct, weakly model-dependent references for isospin systematics and for astrophysical reaction networks [42,141]. Penning-trap facilities such as ISOLTRAP (ISOLDE TRAP), TRIGA-TRAP (Training, Research, Isotopes, General Atomics TRAP), SHIPTRAP (Separator for Heavy Ion reaction Products TRAP), TITAN (TRIUMF's Ion Trap for Atomic and Nuclear science), LEBIT (Low Energy Beam and Ion Trap), and JYFLTRAP (Jyväskylä TRAP) can achieve relative mass uncertainties down to the 10^{-9}–10^{-8} range in favorable cases, while precision for the shortest-lived species is typically limited by cycle time, isomeric contamination, and count-rate systematics [42,142]. These data support Coulomb displacement energies, enable stringent tests of the isobaric multiplet mass equation (IMME), and quantify isospin-symmetry-breaking contributions that must be controlled in precision weak-interaction studies and in global modeling [141]. Storage-ring techniques (isochronous and Schottky mass spectrometry) extend precision mass access to very short-lived nuclides [130–132]. Because the ions are stored and repeatedly observed, storage rings provide access to both masses and decay properties in the same experimental environment, but this advantage comes with calibration-dominated uncertainties. Storage-ring mass extraction is intrinsically calibration-driven: magnetic-rigidity drifts, non-isochronicity corrections, charge-state ambiguities, and acceptance effects must be accounted for [130,131]. In astrophysics, such masses provide key inputs to r-process modeling and to neutron-star crust composition calculations, and they also benchmark global mass models used in broader symmetry-energy systematics [132,141].

3.8. Experimental Limitations and Systematic Uncertainties

Despite substantial experimental progress, studies of nuclear symmetries and symmetry breaking remain constrained by both instrumental effects and interpretative (model-mapping) ambiguities. Improved detector segmentation, fast digital signal processing, and high-granularity tracking have strengthened particle identification and background rejection. Active-target time-projection chambers (TPCs) and related target and vertexing concepts extend sensitivity to low-energy recoils and weakly bound systems by combining large acceptance with low thresholds, but they introduce their own challenges (field non-uniformities, space-charge distortions, gain stability, and efficiency calibration) that must be assessed case by case [108,109]. Machine learning (ML) methods are increasingly applied for event reconstruction, particle classification, detector monitoring, and uncertainty quantification. A core methodological requirement is physics-informed validation: ML-assisted results should be benchmarked against controlled simulations and calibration data [143]. Taken together, the approaches reviewed here provide complementary (often cross-validating) access to nuclear symmetries and their breaking mechanisms. Heavy-ion collisions and charge-exchange reactions primarily inform the density dependence and spin–isospin response; β-decay and γ spectroscopy map isospin structure, collectivity, and shell evolution; precision masses and parity-violating electron scattering provide comparatively model-robust references for binding-energy trends and neutron-density systematics. Figure 1 is a review-wide taxonomy that links symmetry ideas to representative laboratory observables and to the EoS-inference stage; it is an index rather than an inference pipeline. Figure 2 makes the inference workflow explicit, showing how selected laboratory observables are mapped via calibrated theory and uncertainty budgets to nuclear-matter quantities and propagated to neutron-star constraints. Figure 3 places representative probes in a schematic density–temperature plane and highlights an illustrative overlap window.

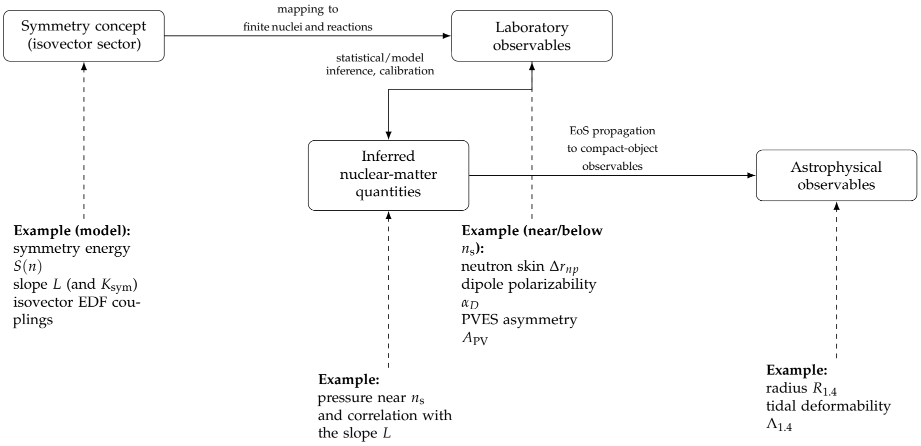

Figure 2. Schematic inference chain linking laboratory observables to neutron-star radii and tidal deformabilities through the isovector sector of the nuclear EoS (illustrated for the symmetry-energy slope L). Solid arrows indicate the main inference/mapping chain, whereas dashed arrows connect illustrative example quantities to the corresponding nodes. Abbreviations: Δr_{np} = neutron-skin thickness; α_D = electric dipole polarizability; PVES = parity-violating electron scattering; A_{PV} = parity-violating asymmetry; $R_{1.4}$ = radius and $\Lambda_{1.4}$ = tidal deformability of a 1.4 $M_\odot$ neutron star.

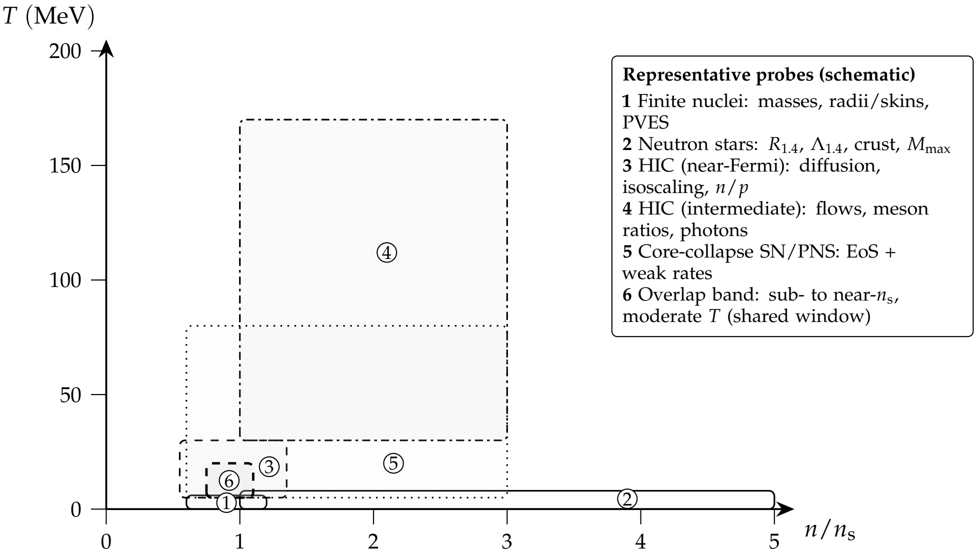

Figure 3. Schematic placement of representative isovector EoS probes in a density–temperature plane. Rectangles indicate illustrative sensitivity regimes rather than sharp experimental boundaries; line styles

encode probe classes: solid = cold constraints (finite nuclei, neutron stars); dashed = near-Fermi heavy-ion collisions (HIC), dash–dot = intermediate-energy HIC, dotted = core-collapse SN/PNS conditions, and the thick dashed box marks an overlap band where finite-nucleus and near-Fermi HIC observables probe related sub- to near-n_s densities at moderate T. Abbreviations: n = baryon density; n_s = saturation density; T = temperature; EoS = equation of state; HIC = heavy-ion collision(s); SN = supernova; PNS = proto-neutron star; PVES = parity-violating electron scattering; n/p = neutron-to-proton (spectral) ratios; $R_{1.4}$ and $\Lambda_{1.4}$ denote the radius and tidal deformability of a 1.4 $M_\odot$ neutron star; $M_{\max}$ is the maximum gravitational mass.

4. Symmetry Energy and Nuclear Astrophysics

The symmetry energy provides a common parametrization for isovector physics in nuclei and neutron-rich matter; however, quantitative links to laboratory observables are obtained through calibrated model correlations and are therefore analysis-conditional. Using the parabolic expansion introduced in Section 1 for homogeneous matter [16,21,25],

$$e(n,\delta) = e(n,0) + S(n)\,\delta^2 + \mathcal{O}(\delta^4), \tag{3}$$

where the isospin asymmetry is $\delta \equiv (n_n - n_p)/n$ and $n = n_n + n_p$. Here, $S(n)$ is the (quadratic) symmetry energy in the parabolic approximation and quantifies the leading isovector contribution, i.e., the energy cost of neutron–proton imbalance at density n [19,20,25]. (If the strong interaction is taken as invariant under $n_n \leftrightarrow n_p$ so that $e(n,\delta) = e(n,-\delta)$, odd powers of δ are absent.) We follow the notation of Equation (1) throughout. At finite temperature, some reaction observables (e.g., fragment yields) are more directly linked to a symmetry free-energy coefficient; unless stated otherwise, we use $S(n)$ for the $T = 0$ energy coefficient and treat finite-T mappings explicitly as model-dependent. While the quadratic term typically dominates near saturation density, higher-order terms can become relevant in very neutron-rich matter and/or at higher density; when extrapolating to neutron-star conditions, such terms should be treated as an explicit source of model-systematic uncertainty and propagated accordingly [144,145]. Several analyses suggest J in the low-30 MeV range and L of order tens of MeV, but quoted intervals remain model- and analysis-conditional, reflecting the adopted framework (EDF, chiral EFT, transport-based inference, or astrophysical Bayesian analyses), data-set selection, and prior assumptions [16,17,21]. Because J–L information is commonly obtained through calibrated correlations (rather than direct inversion), we emphasize the adopted model class, calibration strategy, and dominant systematics when summarizing constraints [16,17,21,25]. As a quantitative complement to the regime map in Figure 3, Figure 4 compiles representative constraints on $S(n)$ as a function of density, illustrating both the probed density windows and the analysis-conditional spread relevant for neutron-star extrapolations.

We first review constraints near and below n_s from neutron densities and isovector response observables in finite nuclei; we then summarize heavy-ion constraints at finite temperature; finally, we connect these inputs to neutron-star structure and multimessenger observables.

Figure 2 sketches how isovector-sector concepts are connected to laboratory observables, mapped (via calibration/inference) to nuclear-matter quantities, and then propagated to neutron-star properties. The middle step relies on model calibration and statistical inference, so correlations must be interpreted together with theoretical and experimental uncertainties. We denote the neutron-skin thickness by Δr_{np}, the electric dipole polarizability by α_D, and the parity-violating electron scattering asymmetry by $A_{\rm PV}$. For neutron-star observables, $R_{1.4}$ and $\Lambda_{1.4}$ denote the radius and tidal deformability of a 1.4 $M_\odot$ star, respectively.

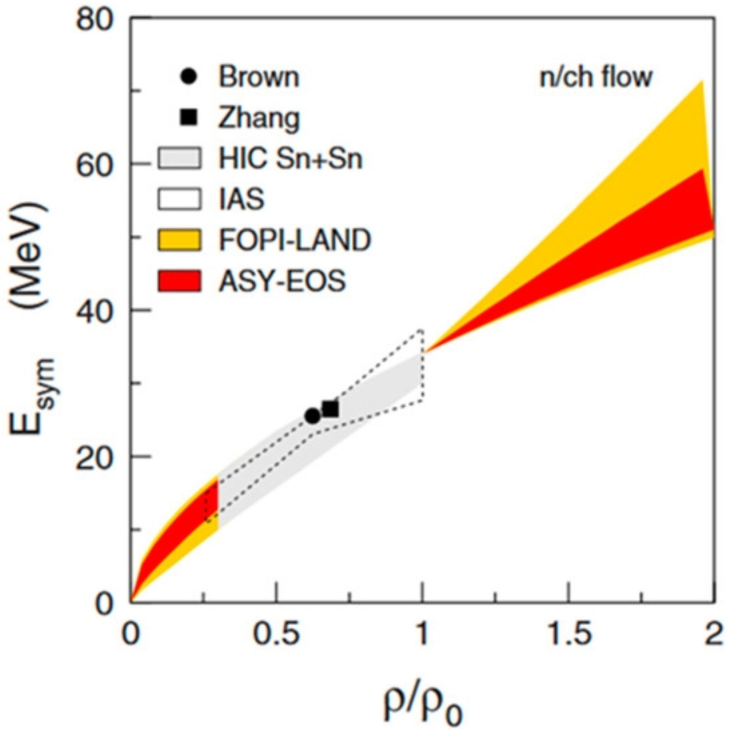

Figure 4. Constraints for the symmetry energy as a function of normalized nuclear density ρ/ρ_0. Legend labels and bands are as in Ref. [146]. As in that reference, the FOPI-LAND and ASY-EOS results are not shown for $0.3 < \rho/\rho_0 < 1.0$. Reproduced from Ref. [146] under CC BY 4.0.

4.1. Symmetry Energy at and Below Saturation Density

Hadronic probes, dipole polarizability measurements, isovector giant resonances, and PVES constrain neutron densities and the isovector response, with differing levels of strong-interaction model dependence [17,21,56]. Neutron-skin thicknesses, defined as the difference between neutron and proton rms radii (e.g., in ^{208}Pb and ^{48}Ca), correlate with the pressure of neutron-rich matter near and below saturation density and, within many model families, with the slope parameter L: larger L often implies thicker skins [17,21,147,148]. Because this mapping is correlation-based within a chosen theory class, the inferred L interval should be quoted together with the EDF/ab initio setup, calibration data, and prior choices [17]. Isobaric analog states, analyzed within charge-invariance assumptions and combined with masses, provide complementary constraints on symmetry-energy coefficients and isospin-breaking systematics (with residual dependence on Coulomb modeling and surface terms) [15]. Systematic studies of the electric dipole polarizability across isotopic chains, combined with EDF and ab initio calculations, support well-characterized correlations between α_D, neutron skins, and the density dependence of the symmetry energy [17,149–151]. Low-lying dipole strength (often discussed in terms of pygmy dipole excitations) can add sensitivity to sub-saturation behavior, although its interpretation is more model-dependent and should be treated accordingly [17,151–153].

4.2. Heavy-Ion Collisions and Symmetry Energy at Finite Temperature

At finite temperature, heavy-ion data constrain the isovector EoS only through transport-model analyses (Section 3); the extracted bands are therefore code- and observable-conditional [82,83,90]. At near-Fermi energies, isospin diffusion in semi-peripheral collisions reflects neutron–proton transport across the low-density neck region. Within transport descriptions, the degree of isospin equilibration is sensitive to the density dependence of the symmetry energy around and below saturation. For many commonly used parameterizations (often quoted at fixed J), a larger L (at fixed J) tends to reduce $S(n)$ at sub-saturation densities when the expansion is anchored at n_s; this can reduce the isovector driving force for isospin diffusion, with the sign and magnitude depending on the transport implementation and on how diffusion is quantified [21,87,88]. Complementary information is provided by isoscaling analyses of fragment yields, which constrain an effective symmetry free-energy coefficient and its temperature dependence; however, the mapping to the underlying symmetry energy depends on assumptions about clustering, secondary decay, and the statistical ensemble [82,83,86]. The synergy between heavy-ion collisions and nuclear structure observables is crucial: structure data constrain the symmetry energy around n_s, while collisions extend sensitivity to finite temperature and, potentially, to supra-saturation densities. The astrophysical relevance is primarily twofold: collisions probe neutron-rich matter away from β equilibrium and at finite T, and they can access densities that overlap with the regime controlling neutron-star radii and tidal deformabilities. Because collisions probe hot, transient matter out of β equilibrium, any astrophysical extrapolation must explicitly account for thermodynamic differences and the framework dependence of the transport-to-EoS mapping [21,90]. We note that the symmetry-linked observables discussed in Section 3 for relativistic heavy-ion collisions primarily probe hot/dense strongly interacting matter. They are complementary to (but not interchangeable with) intermediate-energy constraints on $S(n)$. A particularly transparent bridge between accelerator constraints and multimessenger inference is obtained by recasting both in terms of the pressure of cold neutron-rich matter as a function of density. Figure 5 overlays representative heavy-ion and astrophysical bands in the same (P, ρ) plane, making explicit where laboratory data anchor the EoS (roughly up to $\sim 2\rho_0$) and where uncertainty inflation is dominated by high-density extrapolation.

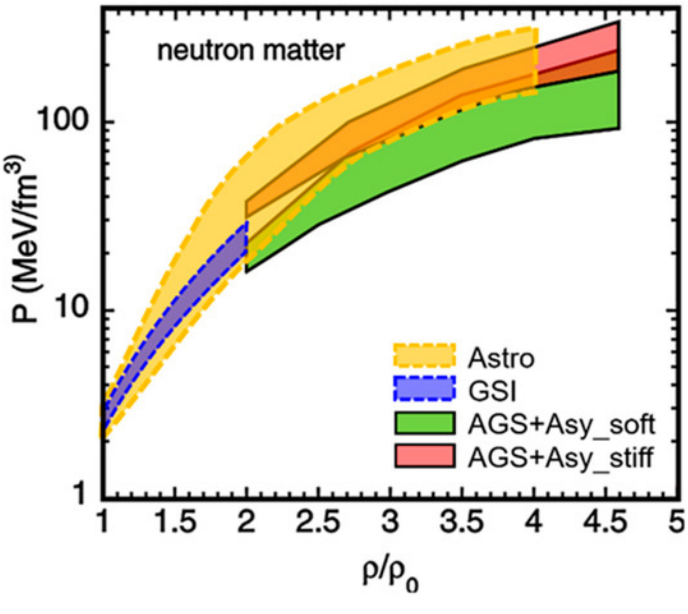

Figure 5. EoS constraints for cold neutron matter shown as pressure versus density. The bands follow Ref. [146]: the orange band ("Astro") is inferred from NICER mass–radius analyses (including massive neutron stars) together with the GW170817 tidal-deformability constraint; the blue band ("GSI") is extracted from GSI flow and kaon data; the green and pink bands ("AGS+Asy_soft" and "AGS+Asy_stiff") are based on AGS flow data with added asymmetry-term pressure for weak and strong density dependence, respectively. Reproduced from Ref. [146] under CC BY 4.0.

4.3. Symmetry Energy, Neutron Stars, and Dense Matter

Neutron stars provide natural laboratories for testing the EoS at densities up to several times saturation, and hence for constraining the symmetry energy within nucleonic and other neutron-rich matter descriptions [22–25,27,29]. To first approximation, a neutron star consists of a neutron-rich crust and a cold, charge-neutral core in β equilibrium [24,25]. In nucleonic descriptions, the isovector sector of the EoS, including the symmetry energy, plays an important role. At higher densities, where additional degrees of freedom may appear, the mapping to a single "symmetry energy" becomes composition dependent and should be stated together with the assumed constituents and parametrization. The mass–radius relation is highly sensitive to the EoS. For a given EoS, the Tolman–Oppenheimer–Volkoff equations yield a family of mass–radius curves. The pressure of β-equilibrated matter at around and moderately above saturation influences the radii of typical neutron stars, while the high-density behavior of the EoS largely determines the maximum supported mass [22,25,29]. Observations of neutron stars with masses close to two solar masses therefore set a robust lower bound on the overall stiffness of the EoS at high density [154,155], although this constraint does not by itself isolate the symmetry-energy contribution. At sub-saturation and near-saturation densities, the symmetry energy and its slope govern the pressure of neutron-rich matter and affect the location of the crust–core transition, crust thickness, and the properties of nuclear "pasta" phases. These features can influence crustal oscillations, glitch phenomenology, and cooling behavior, in combination with pairing and neutrino-emission microphysics [24,25]. The dimensionless tidal deformability measured in gravitational-wave events such as GW170817 is sensitive to stellar compactness and thus to the EoS [27,29]. Analyses of GW170817 have yielded bounds on the tidal deformability of a $1.4\,M_\odot$ neutron star [28], constraining the EoS most robustly at intermediate densities relevant for typical radii; sensitivity to the highest-density regime is more prior and parameterization dependent. While the symmetry energy is only one component of the total pressure, its behavior at around and above saturation remains important for neutron-rich matter, particularly within nucleonic EoS models and when assessing possible composition changes with density. In many recent studies, laboratory constraints on the symmetry energy around saturation density are combined with neutron-star mass–radius and tidal-deformability data in Bayesian frameworks to infer posterior distributions for the EoS (and the implied symmetry energy) over a wide density range [23,25,29,88]. These studies generally suggest a moderately stiffening isovector sector with increasing density within nucleonic models, while significant uncertainties remain at higher densities, where additional degrees of freedom may appear and inference outcomes depend strongly on model choices and priors.

4.4. Multimessenger Constraints and Consistency Across Scales

Multimessenger astrophysics enables cross-checks across systems and helps tighten constraints on the symmetry energy and the EoS. Gravitational waves from compact binary mergers constrain tidal deformability and thus the equation of state [27–29]. Multimessenger analyses, beginning with GW170817 and complemented by NICER pulse-profile modeling, support neutron-star radii of order ∼11–13 km for typical masses in many inference frameworks (with quantitative intervals depending on the assumed EoS parameterization, waveform systematics, and priors) [29,30]. Neutrino and electromagnetic signals from supernovae and kilonovae depend on the EoS and the symmetry energy, although current constraints remain scenario dependent [23,25] and are entangled with additional physics (e.g., neutrino transport, opacities, composition, and magnetic fields). A notable feature of recent studies is the partial consistency between laboratory anchors around n_s and multimessenger inferences at the densities most relevant for typical neutron-star radii within nucleonic

EoS assumptions. Several mappings (e.g., neutron skins → L, tidal deformabilities → L) are correlation-based within a chosen theory class (see Figure 2) [17,21–23,25,27,29,88]. Constraints from finite nuclei, nuclear reactions, and multimessenger observations support a broadly consistent picture of the symmetry energy from sub-saturation densities up to a few times n_s: laboratory data primarily anchor the behavior around n_s, while neutron-star mass–radius and tidal-deformability measurements restrict viable EoS families at higher densities [17,21–23,25,27,29,88]. Significant uncertainties remain at the highest densities, where additional degrees of freedom may appear, but the set of EoS models compatible with current data has narrowed within many commonly used parameterized families and nucleonic/hybrid assumptions since GW170817 [28–30].

5. Precision Symmetry Tests and Frontiers Beyond the Standard Model

So far, we have emphasized how symmetry and symmetry breaking organize nuclear structure and connect finite nuclei to neutron stars. We next consider precision tests at the fundamental level, where extremely small symmetry violations can provide enhanced sensitivity to physics beyond the Standard Model. To limit overlap with the preceding sections, we focus here on symmetry-violating observables whose interpretation hinges on controlled many-body theory and well-quantified uncertainties. In practice, this includes (i) channels whose Standard-Model contributions are absent or extremely suppressed (EDMs and $0\nu\beta\beta$) and (ii) parity-violating observables that are nonzero in the Standard Model but can reveal new physics through precision deviations from controlled electroweak expectations.

Precision studies in nuclei, atoms, and molecules complement searches at high-energy accelerators. High-energy accelerators access new degrees of freedom directly at high momentum transfer, whereas low-energy systems can be highly sensitive to very weak symmetry-violating effects and can probe extremely high effective scales through interference and coherence. In an effective-field-theory language, low-energy observables constrain higher-dimensional operators via coherence and long interrogation times, while collider searches probe the associated dynamics more directly at high momentum transfer.

The primary challenge is interpretation. The discovery potential of EDM, parity-violation, and $0\nu\beta\beta$ programs relies not only on experimental systematics (backgrounds and stability) but also on quantitatively reliable atomic, molecular, and nuclear-structure inputs (many-body correlations, operator renormalization, and uncertainty propagation) [7,8,156,157]. Accordingly, we separate experimental precision from theory-systematic limitations wherever possible (e.g., many-body truncations, operator uncertainties, and model-to-data mappings). Advances in radioactive ion beam production and high-resolution spectroscopy broaden the range of nuclei and molecules that can be exploited for enhanced sensitivity, while electronics developments provide new tools for precision control and readout.

5.1. Time-Reversal Violation and Electric Dipole Moments

A permanent EDM corresponds to a nonzero expectation value of the electric-dipole operator in a stationary state, i.e., a linear energy shift $-\vec{d}\cdot\vec{E}$ in an external electric field. For a spin-polarized system, the relevant observable is the component of $\vec{d}$ along the spin (or total angular momentum) axis, accessed through a P,T-odd linear response to $\vec{E}$. For a non-degenerate stationary state, a nonzero EDM violates both parity (P) and time-reversal (T) symmetries; assuming CPT invariance, this implies CP violation. (In the presence of degeneracies, symmetry arguments require care, but EDM searches still target P,T-odd interactions that induce a linear-in-E response.) Since Standard-Model EDM expectations are many orders of magnitude below present experimental sensitivities, the observation of a nonzero EDM would provide compelling evidence for CP violation beyond the CKM mechanism, potentially arising from, e.g., supersymmetric phases, extended Higgs sectors, leptoquarks, or left–right symmetric interactions [7–9]. Nuclear, atomic, and molecular systems provide particularly stringent EDM probes because symmetry-violating effects can be strongly enhanced by structure and collectivity. In diamagnetic atoms, hadronic CP violation typically enters through nuclear P, T-odd moments (notably Schiff moments), consistent with Schiff screening that suppresses a direct point-like nuclear-EDM contribution in a neutral atom and elevates the role of finite-size and relativistic effects [7,8].

Neutron EDM measurements constrain $|d_n|$ at the $\mathcal{O}(10^{-26})\,e\,\mathrm{cm}$ level (90% C.L.) [158], whereas Standard-Model contributions are expected to be many orders of magnitude smaller. Future efforts aim for one to two orders of magnitude improvement through increased ultracold-neutron statistics, improved magnetic-field control, and reduced systematic effects [7]. A positive signal in any EDM channel would have major implications for particle physics and cosmology, providing a new source of CP violation potentially relevant to the baryon asymmetry of the universe [5,6].

In nuclei with octupole deformation ("pear-shaped" nuclei), parity-doublet structures and collective motion can amplify P, T-odd interactions, leading to enhanced nuclear Schiff moments and, consequently, increased sensitivity of atomic EDMs to hadronic sources of CP violation [159–162]. Isotopes such as ^{225}Ra are therefore prominent candidates for next-generation searches, and the first atomic-EDM measurement in ^{225}Ra has demonstrated the viability of radioactive-atom techniques in this channel [163]. Complementary enhancement mechanisms arise in certain molecules through nuclear P, T-odd moments such as MQMs (magnetic quadrupole moments) [164].

5.2. Neutrinoless Double-β-Decay and Lepton-Number Violation

The standard two-neutrino double-β-decay ($2\nu\beta\beta$) emits two electrons and two antineutrinos and is allowed within the Standard Model. In the neutrinoless mode ($0\nu\beta\beta$), two neutrons transform into two protons and two electrons without neutrino emission. Observation of $0\nu\beta\beta$ would therefore demonstrate lepton-number violation and, in a model-independent sense, imply that neutrinos have a Majorana component (the black-box connection between $0\nu\beta\beta$ and Majorana mass) [165]. $0\nu\beta\beta$ tests whether the neutrino is "its own antiparticle" in the low-energy effective theory. More precisely, any confirmed $0\nu\beta\beta$ signal establishes $\Delta L = 2$ physics and induces a Majorana mass term at some level, even if the dominant microscopic mechanism is not light-neutrino exchange (cf. the black-box argument) [165]. As such, it provides a sensitive probe of lepton-number violation, which is a key ingredient in many scenarios for generating the cosmic matter–antimatter asymmetry (e.g., via leptogenesis), even though the mapping from a low-energy signal to the high-scale origin is mechanism dependent [166,167].

Current leading searches have reached half-life sensitivities at or above the $\gtrsim 10^{26}$ yr scale in benchmark isotopes, notably ^{136}Xe and ^{76}Ge, with the achieved sensitivity set by exposure, background control, and energy resolution [168,169].

LEGEND-1000 (Large Enriched Germanium Experiment for Neutrinoless $\beta\beta$ Decay) and nEXO (next Enriched Xenon Observatory) target sensitivities approaching or exceeding $\sim 10^{28}$ yr, corresponding (for light-neutrino exchange) to effective Majorana masses in the $\mathcal{O}(10)$ meV range, with the exact mapping set by nuclear matrix elements and axial-coupling assumptions [170,171]. Interpreting any $0\nu\beta\beta$ signal (or null result) requires reliable nuclear matrix elements (NMEs), which remain a principal theoretical uncertainty. Complementary indirect constraints on NMEs are being pursued via double charge-exchange reactions, which aim to connect measured strong-interaction amplitudes to the underlying $0\nu\beta\beta$ operators within controlled reaction+structure frameworks [172]. Figure 6 provides an ingredient-level "benchmarking network" in which external observables constrain specific components entering NME calculations (pairing correlations, spin–isospin response, occupancies, and weak operators). State-of-the-art calculations span large-scale shell-model approaches, quasiparticle random-phase approximation, energy-density-functional methods, and emerging ab initio calculations with quantified uncertainties, including efforts based on chiral EFT interactions and consistent weak operators [157,166]. Experimental data including charge-exchange measurements of spin–isospin response and transfer reactions that benchmark pairing and occupancies provide important constraints on key inputs of nuclear-structure descriptions and are increasingly used to validate and discriminate NME frameworks, though they do not fix the full $0\nu\beta\beta$ NME on their own [157].

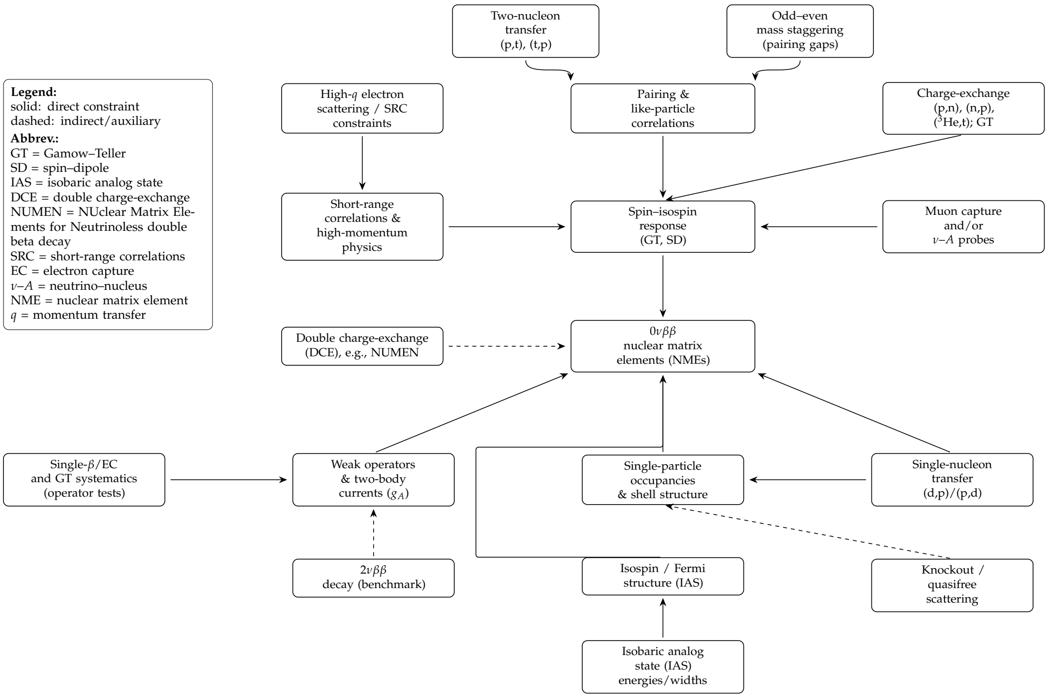

Figure 6. Schematic benchmarking network relating experimental probes to nuclear-structure inputs entering $0\nu\beta\beta$ nuclear matrix elements (NMEs). Solid arrows denote direct constraints; dashed arrows indicate indirect/auxiliary constraints. Abbreviations are listed in the figure. Diagrammatic only (not to scale).

Lastly, although the conventional mechanism is light Majorana neutrino exchange, other short-range or exotic mechanisms (such as heavy sterile neutrino exchange, right-handed currents, or operators mediated by leptoquarks and supersymmetry) may also play a role. Regardless of the predominant underlying mechanism, a confirmed observation would indicate new physics beyond the Standard Model [166,167].

5.3. Parity Violation and Electroweak Symmetry Tests

Parity violation corresponds to interactions that distinguish left from right. Experimentally, it appears as tiny helicity-dependent asymmetries in otherwise ordinary atomic, nuclear, or scattering observables, driven by the chiral structure of the weak interaction. Parity-violating observables provide sensitive low-energy tests of electroweak couplings through interference between electromagnetic and weak amplitudes, complementing collider searches [122–124]. In nuclei, additional parity-violating effects can arise from hadronic weak interactions that mix opposite-parity nuclear states, and in atoms from weak-charge–induced mixing that must be interpreted with high-precision atomic theory [9]. To avoid overlap with Section 3, we emphasize the electroweak “precision-test” aspect: cross-checks of weak charges and the running of $\sin^2\theta_W(Q^2)$ across systems and momentum transfers, rather than neutron-density extraction. Quantitative interpretation requires controlled electroweak radiative corrections and hadronic and atomic-structure inputs [124,128]. Because parity-violating observables are nonzero in the Standard Model, discovery potential comes from statistically significant deviations from the radiatively corrected Standard-Model expectation, or inconsistencies among determinations across Q^2, which elevates the importance of radiative-correction control and theory-error budgets.

5.4. CPT Symmetry and Precision Antimatter Spectroscopy

CPT symmetry states that physics is unchanged under the combined operations of charge conjugation (C), parity (P), and time reversal (T). It is a cornerstone of local, Lorentz-invariant quantum field theory. Under standard assumptions, CPT implies identical masses and (appropriately signed) moments for matter–antimatter counterparts. Atomic and nuclear physics contribute to CPT tests through antihydrogen spectroscopy and Penning-trap comparisons of particle and antiparticle properties. Recent milestones include antihydrogen hyperfine spectroscopy and precision transition measurements in antihydrogen, as well as high-precision proton–antiproton charge-to-mass comparisons and parts-per-billion antiproton magnetic-moment determinations [173–176]. The main challenges are experimental: magnetic-field stability and calibration, trap-related line-shape systematics, and long-term control of correlated drifts. Any statistically significant deviation from CPT invariance would challenge the standard theoretical framework and would require either Lorentz-violation scenarios or departures from conventional quantum field theory assumptions [175,176].

5.5. Radioactive Molecules as Precision Symmetry Probes

Molecules containing heavy (and in some cases radioactive) nuclei combine very large internal effective electric fields with rich level structure. For electron-EDM searches, the relevant quantity is the large effective internal electric field experienced by the valence electron in a polar molecule. These systems amplify symmetry-violating interactions: a very small effect can produce a comparatively large, measurable signal. Heavy polar molecules have enabled leading searches for the electron EDM (e.g., ThO) and complementary measurements with trapped molecular ions (e.g., HfF^+), while radioactive molecules such as RaF are promising for enhanced sensitivity to hadronic CP violation through nuclear Schiff moments [177–180].

5.6. Future Directions in Symmetry Tests

In our opinion, future developments in nuclear symmetry tests will be supported more by sustained improvements in experimental sensitivity and theoretical interpretation than by the introduction of new symmetry notions. In the search for time-reversal and CP violation, EDM experiments are expected to remain a central focus. Improvements in source intensity, trapping efficiency, magnetic-field stability, and background rejection will contribute to enhanced sensitivity. The most promising gains are expected in heavy atoms and molecules and in octupole nuclei, where electronic and collective nuclear structure can amplify CP-odd interactions (e.g., via enhanced Schiff moments) [7–9,164]. As half-life sensitivities for neutrinoless double-β-decay move toward and beyond 10^{28} years, interpretation becomes increasingly limited by nuclear-structure inputs (matrix elements and effective axial coupling), supporting coordinated programs that combine decay searches with charge-exchange and two-nucleon transfer constraints and with modern many-body calculations, including chiral-EFT-informed approaches [157,166,167]. Advances in atomic and molecular spectroscopy, particularly in heavy systems, will further expand precision access to parity- and CP-violating observables through level shifts and transition amplitudes that can be extremely difficult to reach in nuclear experiments alone [7,9]. As experimental sensitivities advance, the limiting factor in many symmetry tests will not be the ability to measure small effects, but the confidence with which those effects can be traced back to specific underlying interactions [7,8]. Across all of these areas, progress will depend as strongly on theory as on experiment. Improved uncertainty quantification in nuclear many-body calculations, clearer connections between effective-field-theory interactions and measured observables, and consistent treatments of symmetry breaking and restoration are crucial for drawing robust conclusions from increasingly precise data.

6. Conclusions

This review has emphasized symmetry as a unifying notion in nuclear physics, offering a common framework for phenomena ranging from searches for physics beyond the Standard Model to the structure of finite nuclei and neutron-star properties, including the inference chains and dominant systematics that connect these domains. Approximate symmetries in nuclei, including isospin, pseudospin, and collective dynamical symmetries associated with SU(3) and $\mathrm{Sp}(3,\mathbb{R})$, play a central role in shaping spectra, transition patterns, and emergent regularities. Their systematic breaking through Coulomb effects, shell evolution, continuum coupling, and spin–orbit coupling is more than a complication: it provides detailed and often quantitative information on the effective nuclear interaction and correlated many-body motion.

Recent advances in high-resolution γ spectroscopy, charge-exchange reactions, precision mass measurements, and radioactive-ion-beam experiments have improved our ability to isolate and quantify these effects, especially far from stability where weak binding and strong isospin asymmetry amplify both symmetry-breaking signatures and sensitivity to structural detail. At the macroscopic level, the nuclear symmetry energy provides a quantitative bridge between finite nuclei and neutron-rich matter in astrophysical environments. Constraints from neutron skins, dipole polarizability, and heavy-ion collisions are increasingly interpreted alongside those inferred from neutron-star mass–radius measurements, tidal deformabilities from gravitational waves, and X-ray timing. This emerging convergence has begun to narrow the range of feasible equations of state near saturation density in many contemporary analyses, and often favors moderately stiff isovector behavior within nucleonic EoS families. In practice, most constraints enter through calibrated correlations rather than direct inversion, so quoted EoS intervals should be interpreted together with the assumed parameterization, composition, and calibration/prior choices. Important uncertainties persist at supra-saturation densities, where additional degrees of freedom and phase transitions may become relevant and where inference outcomes can become strongly prior- and parameterization-dependent. Nuclear, atomic, and molecular systems can amplify extremely small symmetry-violating effects and thereby provide sensitive probes of CP violation and physics beyond the Standard Model. Searches for electric dipole moments, neutrinoless double-β-decay, and parity-violating observables continue to push experimental sensitivity into regimes that are complementary to high-energy collider probes. The limiting factor is not only the measurement itself but the confidence with which a null result or discovery can be traced back to specific underlying operators, given nuclear, atomic, and hadronic-structure uncertainties. This emphasizes the need for nuclear many-body theory with controlled theoretical errors and transparent uncertainty quantification. Next-generation rare-isotope facilities will extend experimental reach toward the most neutron-rich and proton-rich systems, while continued improvements in detector technology, beam delivery, and data-analysis methods will reduce systematic uncertainties that currently limit symmetry-based constraints. On the theory side, sustained integration of ab initio approaches, EDF methods, and astrophysical modeling with consistent treatments of symmetry breaking and restoration and with uncertainty-quantified links between theory and data will be needed to maintain coherence between laboratory observables and dense-matter phenomenology.

Near-term decisive measurements and developments:

- Electroweak neutron-density anchors (PVES and related probes), combined with α_D in calibrated EDF/ab initio analyses, to sharpen the mapping to L around n_s with explicitly propagated theoretical and calibration uncertainties.
- Inter-code benchmarks and uncertainty-quantified transport analyses of heavy-ion observables (momentum dependence, in-medium cross sections, clustering, meson potentials) to improve the robustness and comparability of supra-saturation isovector constraints across model classes.
- Multimessenger neutron-star inference with reduced waveform/emission systematics, explicit consistency tests against laboratory anchors around n_s, and marginalization over composition/phase-transition uncertainties, including quantified prior sensitivity.
- Coordinated $0\nu\beta\beta$ benchmarking across isotopes, with cross-checks from charge-exchange and transfer/spectroscopy, to help reduce NME-driven systematics in BSM reach and interpretation.

Symmetry provides more than classification: it links disparate observables, identifies robust correlations, and clarifies where current models and inference strategies introduce dominant systematics. By investigating when symmetries hold and how they fail, nuclear physics offers insight into the structure of matter and the governing interactions across scales, from nuclei to neutron stars.

Funding: This research was funded by Slovenian Research and Innovation Agency, grant numbers: P1-0102, I0-E005.

Data Availability Statement: No new data were created or analyzed in this study.

Conflicts of Interest: The author declares no conflict of interest.

References

1. Noether, E. Invariante Variationsprobleme. *Nachrichten Ges. Wiss. Göttingen Math.-Phys. Kl.* **1918**, *1918*, 235–257.
2. Navas, S.; Amsler, C.; Gutsche, T.; Hanhart, C.; Hernández-Rey, J.J.; Lourenço, C.; Masoni, A.; Mikhasenko, M.; Mitchell, R.E.; Patrignani, C.; et al. Review of Particle Physics. *Phys. Rev. D* **2024**, *110*, 030001. [CrossRef]
3. Lee, T.D.; Yang, C.N. Question of Parity Conservation in Weak Interactions. *Phys. Rev.* **1956**, *104*, 254–258. [CrossRef]
4. Wu, C.S.; Ambler, E.; Hayward, R.W.; Hoppes, D.D.; Hudson, R.P. Experimental Test of Parity Conservation in Beta Decay. *Phys. Rev.* **1957**, *105*, 1413–1415. [CrossRef]
5. Dine, M.; Kusenko, A. The Origin of the Matter–Antimatter Asymmetry. *Rev. Mod. Phys.* **2003**, *76*, 1–30. [CrossRef]
6. Riotto, A.; Trodden, M. Recent Progress in Baryogenesis. *Annu. Rev. Nucl. Part. Sci.* **1999**, *49*, 35–75. [CrossRef]
7. Chupp, T.E.; Fierlinger, P.; Ramsey-Musolf, M.J.; Singh, J.T. Electric dipole moments of atoms, molecules, nuclei, and particles. *Rev. Mod. Phys.* **2019**, *91*, 015001. [CrossRef]
8. Engel, J.; Ramsey-Musolf, M.J.; van Kolck, U. Electric Dipole Moments of Nucleons, Nuclei, and Atoms: The Standard Model and Beyond. *Prog. Part. Nucl. Phys.* **2013**, *71*, 21–74. [CrossRef]
9. Safronova, M.S.; Budker, D.; DeMille, D.; Kimball, D.F.J.; Derevianko, A.; Clark, C.W. Search for New Physics with Atoms and Molecules. *Rev. Mod. Phys.* **2018**, *90*, 025008. [CrossRef]
10. Heisenberg, W. Über den Bau der Atomkerne. I. *Z. Phys.* **1932**, *77*, 1–11. [CrossRef]
11. Wigner, E.P. On the Consequences of the Symmetry of the Nuclear Hamiltonian on the Spectroscopy of Nuclei. *Phys. Rev.* **1937**, *51*, 106–119. [CrossRef]
12. Miller, G.A.; Opper, A.K.; Stephenson, E.J. Charge Symmetry Breaking and QCD. *Annu. Rev. Nucl. Part. Sci.* **2006**, *56*, 253–292. [CrossRef]
13. Bentley, M.A.; Lenzi, S.M. Coulomb energy differences between high-spin states in isobaric multiplets. *Prog. Part. Nucl. Phys.* **2007**, *59*, 497–561. [CrossRef]
14. MacCormick, M.; Audi, G. Evaluated Experimental Isobaric Analogue States from T = 1/2 to T = 3 and Associated IMME Coefficients. *Nucl. Phys. A* **2014**, *925*, 61–95. [CrossRef]

15. Danielewicz, P.; Lee, J. Symmetry energy II: Isobaric analog states. *Nucl. Phys. A* **2014**, *922*, 1–70. [CrossRef]
16. Lattimer, J.M.; Lim, Y. Constraining the symmetry parameters of the nuclear interaction. *Astrophys. J.* **2013**, *771*, 51. [CrossRef]
17. Roca-Maza, X.; Paar, N. Nuclear Equation of State from Ground and Collective Excited State Properties of Nuclei. *Prog. Part. Nucl. Phys.* **2018**, *101*, 96–176. [CrossRef]
18. Dieperink, A.E.L.; van Isacker, P. The symmetry energy in nuclei and in nuclear matter. *Eur. Phys. J. A* **2007**, *32*, 11–18. [CrossRef]
19. Hebeler, K.; Holt, J.D.; Menéndez, J.; Schwenk, A. Nuclear Forces and Their Impact on Neutron-Rich Nuclei and Neutron-Rich Matter. *Annu. Rev. Nucl. Part. Sci.* **2015**, *65*, 457–484. [CrossRef]
20. Drischler, C.; Furnstahl, R.J.; Meléndez, J.A.; Phillips, D.R. How Well Do We Know the Neutron-Matter Equation of State at the Densities Inside Neutron Stars? A Bayesian Approach with Correlated Uncertainties. *Phys. Rev. Lett.* **2020**, *125*, 202702. [CrossRef] [PubMed]
21. Tsang, M.B.; Stone, J.R.; Camera, F.; Danielewicz, P.; Gandolfi, S.; Hebeler, K.; Horowitz, C.J.; Lee, J.; Lynch, W.G.; Kohley, Z.; et al. Constraints on the symmetry energy and neutron skins from experiments and theory. *Phys. Rev. C* **2012**, *86*, 015803. [CrossRef]
22. Lattimer, J.M.; Steiner, A.W. Constraints on the Symmetry Energy Using the Mass-Radius Relation of Neutron Stars. *Eur. Phys. J. A* **2014**, *50*, 40. [CrossRef]
23. Li, B.A.; Krastev, P.G.; Wen, D.H.; Zhang, N.B. Towards Understanding the Astrophysical Effects of Nuclear Symmetry Energy. *Eur. Phys. J. A* **2019**, *55*, 117. [CrossRef]
24. Lattimer, J.M.; Prakash, M. The Physics of Neutron Stars. *Science* **2004**, *304*, 536–542. [CrossRef]
25. Oertel, M.; Hempel, M.; Klähn, T.; Typel, S. Equations of State for Supernovae and Compact Stars. *Rev. Mod. Phys.* **2017**, *89*, 015007. [CrossRef]
26. Fattoyev, F.J.; Piekarewicz, J.; Horowitz, C.J. Neutron Skins and Neutron Stars in the Multimessenger Era. *Phys. Rev. Lett.* **2018**, *120*, 172702. [CrossRef]
27. Abbott, B.P.; Abbott, R.; Abbott, T.D.; Acernese, F.; Ackley, K.; Adams, C.; Adams, T.; Addesso, P.; Adhikari, R.X.; Adya, V.B.; et al. GW170817: Observation of Gravitational Waves from a Binary Neutron Star Inspiral. *Phys. Rev. Lett.* **2017**, *119*, 161101. [CrossRef]
28. Abbott, B.P.; Abbott, R.; Abbott, T.D.; Acernese, F.; Ackley, K.; Adams, C.; Adams, T.; Addesso, P.; Adhikari, R.X.; Adya, V.B.; et al. GW170817: Measurements of Neutron Star Radii and Equation of State. *Phys. Rev. Lett.* **2018**, *121*, 161101. [CrossRef]
29. Annala, E.; Gorda, T.; Kurkela, A.; Vuorinen, A. Gravitational-Wave Constraints on the Neutron-Star-Matter Equation of State. *Phys. Rev. Lett.* **2018**, *120*, 172703. [CrossRef]
30. Riley, T.E.; Watts, A.L.; Bogdanov, S.; Ray, P.S.; Guillot, S.; Arzoumanian, Z.; Ballantyne, D.R.; Belloni, T.; Bhattacharyya, S.; Bilous, A.V.; et al. A NICER View of PSR J0030+0451: Millisecond Pulsar Parameter Estimation. *Astrophys. J. Lett.* **2019**, *887*, L21. [CrossRef]
31. Li, B.-A.; Chen, L.-W. Neutron–proton effective mass splitting in neutron-rich matter and its impacts on nuclear reactions. *Mod. Phys. Lett. A* **2015**, *30*, 1530010. [CrossRef]
32. Li, X.-H.; Guo, W.-J.; Li, B.-A.; Chen, L.-W.; Fattoyev, F.J.; Newton, W.G. Neutron–proton effective mass splitting in neutron-rich matter at normal density from analyzing nucleon–nucleus scattering data within an isospin dependent optical model. *Phys. Lett. B* **2015**, *743*, 408–414. [CrossRef]
33. Fujita, Y.; Rubio, B.; Gelletly, W. Spin–isospin excitations probed by strong, weak and electromagnetic interactions. *Prog. Part. Nucl. Phys.* **2011**, *66*, 549–606. [CrossRef]
34. Fujita, Y.; Fujita, H.; Rubio, B.; Gelletly, W.; Blank, B. Gamow–Teller Transitions—A Mirror Reflecting Nuclear Structure. *Acta Phys. Pol. B* **2012**, *43*, 153–166. [CrossRef]
35. Fujita, H.; Fujita, Y.; Adachi, T.; Akimune, H.; Botha, N.T.; Hatanaka, K.; Matsubara, H.; Nakanishi, K.; Neveling, R.; Okamoto, A.; et al. Isospin mixing of the isobaric analog state studied in a high-resolution ^{56}Fe(^{3}He,t)^{56}Co reaction. *Phys. Rev. C* **2013**, *88*, 054329. [CrossRef]
36. Diel, F.; Fujita, Y.; Fujita, H.; Cappuzzello, F.; Ganioğlu, E.; Grewe, E.-W.; Hashimoto, T.; Hatanaka, K.; Honma, M.; Itoh, T.; et al. High-resolution study of the Gamow–Teller (GT^{-}) strength in the ^{64}Zn(^{3}He,t)^{64}Ga reaction. *Phys. Rev. C* **2019**, *99*, 054322. [CrossRef]
37. Litvinov, Y.A.; Bosch, F. Beta decay of highly charged ions. *Rep. Prog. Phys.* **2011**, *74*, 016301. [CrossRef]
38. Horowitz, C.J.; Ahmed, Z.; Jen, C.-M.; Rakhman, A.; Souder, P.A.; Dalton, M.M.; Liyanage, N.; Paschke, K.D.; Saenboonruang, K.; Silwal, R.; et al. Weak Charge Form Factor and Radius of ^{208}Pb through Parity Violation in Electron Scattering. *Phys. Rev. C* **2012**, *85*, 032501. [CrossRef]
39. Stephanov, M.A.; Rajagopal, K.; Shuryak, E.V. Event-by-Event Fluctuations in Heavy Ion Collisions and the QCD Critical Point. *Phys. Rev. D* **1999**, *60*, 114028. [CrossRef]
40. Stephanov, M.A. QCD Phase Diagram and the Critical Point. *Int. J. Mod. Phys. A* **2005**, *20*, 4387–4392. [CrossRef]
41. Stephanov, M.A. Non-Gaussian Fluctuations near the QCD Critical Point. *Phys. Rev. Lett.* **2009**, *102*, 032301. [CrossRef]
42. Blaum, K. High-accuracy mass spectrometry with stored ions. *Phys. Rep.* **2006**, *425*, 1–78. [CrossRef]

43. Campbell, P.; Moore, I.D.; Pearson, M.R. Laser spectroscopy for nuclear structure physics. *Prog. Part. Nucl. Phys.* **2016**, *86*, 127–180. [CrossRef]
44. Palit, R.; Saha, S.; Sethi, J.; Trivedi, T.; Sharma, S.; Naidu, B.S.; Jadhav, S.; Donthi, R.; Chavan, P.B.; Tan, H.; et al. A high-speed digital data acquisition system for the Indian National Gamma Array at Tata Institute of Fundamental Research. *Nucl. Instrum. Methods Phys. Res. A* **2012**, *680*, 90–96. [CrossRef]
45. Korten, W.; Atac, A.; Beaumel, D.; Bednarczyk, P.; Bentley, M.A.; Benzoni, G.; Boston, A.; Bracco, A.; Cederkäll, J.; Cederwall, B.; et al. Physics opportunities with the Advanced Gamma Tracking Array: AGATA. *Eur. Phys. J. A* **2020**, *56*, 137. [CrossRef]
46. Epelbaum, E.; Hammer, H.-W.; Meißner, U.-G. Modern Theory of Nuclear Forces. *Rev. Mod. Phys.* **2009**, *81*, 1773–1825. [CrossRef]
47. Van Isacker, P.; Heyde, K.; Jolie, J.; Sevrin, A. The F-spin symmetric limits of the neutron-proton interacting boson model. *Ann. Phys.* **1986**, *171*, 253–296. [CrossRef]
48. Iachello, F.; Arima, A. *The Interacting Boson Model*; Cambridge University Press: Cambridge, UK, 1987.
49. Ginocchio, J.N. Pseudospin as a Relativistic Symmetry. *Phys. Rev. Lett.* **1997**, *78*, 436–439. [CrossRef]
50. Lüders, G. On the Equivalence of Invariance under Time Reversal and under Particle–Antiparticle Conjugation for Relativistic Field Theories. *Dan. Mat. Fys. Medd.* **1954**, *28*, 1–17.
51. Pauli, W. Exclusion Principle, Lorentz Group and Reflection of Space-Time and Charge. In *Niels Bohr and the Development of Physics*; Pauli, W., Ed.; Pergamon Press: London, UK, 1955; pp. 30–51.
52. Elliott, J.P. Collective Motion in the Nuclear Shell Model. I. Classification Schemes for States of Mixed Configurations. *Proc. R. Soc. Lond. A* **1958**, *245*, 128–145. [CrossRef]
53. Elliott, J.P. Collective Motion in the Nuclear Shell Model. II. The Introduction of Intrinsic Wave-Functions. *Proc. R. Soc. Lond. A* **1958**, *245*, 562–581. [CrossRef]
54. Rowe, D.J.; Wood, J.L. *Fundamentals of Nuclear Models: Foundational Models*; World Scientific: Singapore, 2010. [CrossRef]
55. Launey, K.D.; Dytrych, T.; Draayer, J.P. Symmetry-Guided Large-Scale Shell-Model Theory. *Prog. Part. Nucl. Phys.* **2016**, *89*, 101–136. [CrossRef]
56. Harakeh, M.N.; van der Woude, A. *Giant Resonances: Fundamental High-Frequency Modes of Nuclear Excitation*; Oxford University Press: Oxford, UK, 2001; ISBN 978-0-19-851733-7.
57. Garg, U.; Colò, G. The Compression-Mode Giant Resonances and Nuclear Incompressibility. *Prog. Part. Nucl. Phys.* **2018**, *101*, 55–95. [CrossRef]
58. Auerbach, N. Coulomb Effects in Nuclear Structure. *Phys. Rep.* **1983**, *98*, 273–341. [CrossRef]
59. Sun, L.J.; Xu, X.X.; Lin, C.J.; Lee, J.; Hou, S.Q.; Yuan, C.X.; Li, Z.H.; José, J.; He, J.J.; Wang, J.S.; et al. β-decay spectroscopy of ^{27}S. *Phys. Rev. C* **2019**, *99*, 064312. [CrossRef]
60. Bender, M.; Heenen, P.-H.; Reinhard, P.-G. Self-consistent mean-field models for nuclear structure. *Rev. Mod. Phys.* **2003**, *75*, 121–180. [CrossRef]
61. Ehrman, J.B. On the Displacement of Corresponding Energy Levels of ^{13}C and ^{13}N. *Phys. Rev.* **1951**, *81*, 412–416. [CrossRef]
62. Thomas, R.G. An Analysis of the Energy Levels of the Mirror Nuclei, ^{13}C and ^{13}N. *Phys. Rev.* **1952**, *88*, 1109–1125. [CrossRef]
63. Bentley, M.A.; Lenzi, S.M.; Simpson, S.A.; Diget, C.A. Isospin-Breaking Interactions Studied through Mirror Energy Differences. *Phys. Rev. C* **2015**, *92*, 024310. [CrossRef]
64. Pfützner, M.; Karny, M.; Grigorenko, L.V.; Riisager, K. Radioactive Decays at Limits of Nuclear Stability. *Rev. Mod. Phys.* **2012**, *84*, 567–619. [CrossRef]
65. Ginocchio, J.N. Relativistic symmetries in nuclei and hadrons. *Phys. Rep.* **2005**, *414*, 165–261. [CrossRef]
66. Liang, H.; Meng, J.; Zhou, S.-G. Hidden Pseudospin and Spin Symmetries and Their Origins in Atomic Nuclei. *Phys. Rep.* **2015**, *570*, 1–84. [CrossRef]
67. Pietralla, N.; von Brentano, P.; Lisetskiy, A.F. Experiments on multiphonon states with proton–neutron mixed symmetry in vibrational nuclei. *Prog. Part. Nucl. Phys.* **2008**, *60*, 225–282. [CrossRef]
68. Hennig, A.; Spieker, M.; Werner, V.; Ahn, T.; Anagnostatou, V.; Cooper, N.; Derya, V.; Elvers, M.; Endres, J.; Goddard, P.; et al. Mixed-Symmetry Octupole and Hexadecapole Excitations in the $N = 52$ Isotones. *Phys. Rev. C* **2014**, *90*, 051302(R). [CrossRef]
69. Coquard, L.; Pietralla, N.; Rainovski, G.; Ahn, T.; Bettermann, L.; Carpenter, M.P.; Janssens, R.V.F.; Leske, J.; Lister, C.J.; Möller, O.; et al. Evolution of the mixed-symmetry $2^+_{1,\mathrm{ms}}$ quadrupole-phonon excitation from spherical to γ-soft Xe nuclei. *Phys. Rev. C* **2010**, *82*, 024317. [CrossRef]
70. Frederico, T.; Delfino, A.; Tomio, L.; Yamashita, M.T. Universal Aspects of Light Halo Nuclei. *Prog. Part. Nucl. Phys.* **2012**, *67*, 939–994. [CrossRef]
71. Freer, M.; Horiuchi, H.; Kanada-En'yo, Y.; Lee, D.; Meißner, U.-G. Microscopic Clustering in Light Nuclei. *Rev. Mod. Phys.* **2018**, *90*, 035004. [CrossRef]
72. Heyde, K.; Wood, J.L. Shape Coexistence in Atomic Nuclei. *Rev. Mod. Phys.* **2011**, *83*, 1467–1521. [CrossRef]
73. Frauendorf, S.; Macchiavelli, A.O. Overview of neutron–proton pairing. *Prog. Part. Nucl. Phys.* **2014**, *78*, 24–90. [CrossRef]

74. Cederwall, B.; Ghazi Moradi, F.; Bäck, T.; Johnson, A.; Blomqvist, J.; Clément, E.; de France, G.; Wadsworth, R.; Andgren, K.; Lagergren, K.; et al. Evidence for a spin-aligned neutron–proton paired phase from the level structure of ^{92}Pd. *Nature* **2011**, *469*, 68–71. [CrossRef]
75. Talmi, I. *Simple Models of Complex Nuclei: The Shell Model and Interacting Boson Model*; Harwood Academic Publishers: Chur, Switzerland, 1993.
76. Hammer, H.-W.; König, S.; van Kolck, U. Nuclear Effective Field Theory: Status and Perspectives. *Rev. Mod. Phys.* **2020**, *92*, 025004. [CrossRef]
77. Weinberg, S. Nuclear Forces from Chiral Lagrangians. *Phys. Lett. B* **1990**, *251*, 288–292. [CrossRef]
78. Weinberg, S. Effective Chiral Lagrangians for Nucleon–Pion Interactions and Nuclear Forces. *Nucl. Phys. B* **1991**, *363*, 3–18. [CrossRef]
79. Machleidt, R.; Entem, D.R. Chiral Effective Field Theory and Nuclear Forces. *Phys. Rep.* **2011**, *503*, 1–75. [CrossRef]
80. Krebs, H. Nuclear currents in chiral effective field theory. *Eur. Phys. J. A* **2020**, *56*, 234. [CrossRef]
81. Ring, P.; Schuck, P. *The Nuclear Many-Body Problem*; Texts and Monographs in Physics; Springer: Berlin/Heidelberg, Germany, 1980; ISBN 3-540-09820-8.
82. Li, B.A.; Chen, L.W.; Ko, C.M. Recent Progress and New Challenges in Isospin Physics with Heavy-Ion Reactions. *Phys. Rep.* **2008**, *464*, 113–281. [CrossRef]
83. Baran, V.; Colonna, M.; Greco, V.; Di Toro, M. Reaction dynamics with exotic nuclei. *Phys. Rep.* **2005**, *410*, 335–466. [CrossRef]
84. Aumann, T.; Bertulani, C.A.; Schindler, F.; Typel, S. Peeling Off Neutron Skins from Neutron-Rich Nuclei: Constraints on the Symmetry Energy from Neutron-Removal Cross Sections. *Phys. Rev. Lett.* **2017**, *119*, 262501. [CrossRef]
85. Danielewicz, P.; Lacey, R.; Lynch, W.G. Determination of the Equation of State of Dense Matter. *Science* **2002**, *298*, 1592–1596. [CrossRef]
86. Tsang, M.B.; Friedman, W.A.; Gelbke, C.K.; Lynch, W.G.; Verde, G.; Xu, H.S. Isotopic scaling in nuclear reactions. *Phys. Rev. Lett.* **2001**, *86*, 5023–5026. [CrossRef]
87. Tsang, M.B.; Liu, T.X.; Shi, L.; Danielewicz, P.; Gelbke, C.K.; Liu, X.D.; Lynch, W.G.; Tan, W.P.; Verde, G.; Wagner, A.; et al. Isospin diffusion and the nuclear symmetry energy in heavy-ion reactions. *Phys. Rev. Lett.* **2004**, *92*, 062701. [CrossRef]
88. Li, B.-A.; Ramos, À.; Verde, G.; Vidaña, I. Topical Issue on Nuclear Symmetry Energy. *Eur. Phys. J. A* **2014**, *50*, 9. [CrossRef]
89. Xu, J.; Chen, L.-W.; Tsang, M.B.; Wolter, H.; Zhang, Y.-X.; Aichelin, J.; Colonna, M.; Cozma, D.; Danielewicz, P.; Feng, Z.-Q.; et al. Understanding transport simulations of heavy-ion collisions at 100 and 400 AMeV: Comparison of heavy-ion transport codes under controlled conditions. *Phys. Rev. C* **2016**, *93*, 044609. [CrossRef]
90. Lynch, W.G.; Tsang, M.B. Decoding the density dependence of the nuclear symmetry energy. *Phys. Lett. B* **2022**, *830*, 137098. [CrossRef]
91. Xiao, Z.; Li, B.-A.; Chen, L.-W.; Yong, G.-C.; Zhang, M. Circumstantial Evidence for a Soft Nuclear Symmetry Energy at Suprasaturation Densities. *Phys. Rev. Lett.* **2009**, *102*, 062502. [CrossRef] [PubMed]
92. Xiao, Z.-G.; Yong, G.-C.; Chen, L.-W.; Li, B.-A.; Zhang, M.; Xiao, G.-Q.; Xu, N. Probing Nuclear Symmetry Energy at High Densities Using Pion, Kaon, Eta and Photon Productions in Heavy-Ion Collisions. *Eur. Phys. J. A* **2014**, *50*, 37. [CrossRef]
93. Cozma, M.D. Constraining the density dependence of the symmetry energy using the multiplicity and average p_T ratios of charged pions. *Phys. Rev. C* **2017**, *95*, 014601. [CrossRef]
94. Ferini, G.; Gaitanos, T.; Colonna, M.; Di Toro, M.; Wolter, H.H. Isospin Effects on Subthreshold Kaon Production at Intermediate Energies. *Phys. Rev. Lett.* **2006**, *97*, 202301. [CrossRef]
95. Yong, G.-C.; Li, B.-A.; Chen, L.-W. Neutron–Proton Bremsstrahlung from Intermediate-Energy Heavy-Ion Reactions as a Probe of the Nuclear Symmetry Energy? *Phys. Lett. B* **2008**, *661*, 82–87. [CrossRef]
96. Heinz, U.; Snellings, R. Collective flow and viscosity in relativistic heavy-ion collisions. *Annu. Rev. Nucl. Part. Sci.* **2013**, *63*, 123–151. [CrossRef]
97. Becattini, F.; Buzzegoli, M.; Niida, T.; Pu, S.; Tang, A.-H.; Wang, Q. Spin polarization in relativistic heavy-ion collisions. *Int. J. Mod. Phys. E* **2024**, *33*, 2430006. [CrossRef]
98. Russotto, P.; Gannon, S.; Kupny, S.; Lasko, P.; Acosta, L.; Adamczyk, M.; Al-Ajlan, A.; Al-Garawi, M.; Al-Homaidhi, S.; Amorini, F.; et al. Results of the ASY-EOS experiment at GSI: The symmetry energy at suprasaturation density. *Phys. Rev. C* **2016**, *94*, 034608. [CrossRef]
99. Kobayashi, T.; Chiga, N.; Isobe, T.; Kondo, Y.; Kubo, T.; Kusaka, K.; Motobayashi, T.; Nakamura, T.; Ohnishi, J.; Okuno, H.; et al. SAMURAI Spectrometer for RI Beam Experiments. *Nucl. Instrum. Methods Phys. Res. B* **2013**, *317*, 294–304. [CrossRef]
100. Hong, B.; Ahn, D.S.; Ahn, J.K.; Bae, J.; Bae, Y.; Bok, J.S.; Choi, S.W.; Do, S.; Heo, C.; Huh, J.; et al. Status of LAMPS at RAON. *Nucl. Instrum. Methods Phys. Res. B* **2023**, *541*, 260–263. [CrossRef]
101. Taddeucci, T.N.; Goulding, C.A.; Carey, T.A.; Byrd, R.C.; Goodman, C.D.; Gaarde, C.; Larsen, J.; Horen, D.; Rapaport, J.; Sugarbaker, E. The (p,n) reaction as a probe of beta decay strength. *Nucl. Phys. A* **1987**, *469*, 125–172. [CrossRef]
102. Osterfeld, F. Nuclear spin and isospin excitations. *Rev. Mod. Phys.* **1992**, *64*, 491–557. [CrossRef]

103. Ichimura, M.; Sakai, H.; Wakasa, T. Spin–isospin responses via (p,n) and (n,p) reactions. *Prog. Part. Nucl. Phys.* **2006**, *56*, 446–531. [CrossRef]
104. Langanke, K.; Martínez-Pinedo, G. Nuclear Weak-Interaction Processes in Stars. *Rev. Mod. Phys.* **2003**, *75*, 819–862. [CrossRef]
105. Fujiwara, M.; Akimune, H.; Daito, I.; Fujimura, H.; Fujita, Y.; Hatanaka, K.; Ikegami, H.; Katayama, I.; Nagayama, K.; Matsuoka, N.; et al. Magnetic Spectrometer Grand Raiden. *Nucl. Instrum. Methods Phys. Res. A* **1999**, *422*, 484–488. [CrossRef]
106. Shimbara, Y.; Fujita, Y.; Adachi, T.; Berg, G.P.A.; Fujimura, H.; Fujita, H.; Fujita, K.; Hara, K.; Hara, K.Y.; Hatanaka, K.; et al. High-resolution study of Gamow–Teller transitions with the ^{37}Cl(^{3}He,t)^{37}Ar reaction. *Phys. Rev. C* **2012**, *86*, 024312. [CrossRef]
107. Neveling, R. Opportunities with the K600 Magnetic Spectrometer During Phase 1 of the iThemba LABS RIB Project. In *Exotic Nuclei IASEN-2013, Proceedings of the First International African Symposium on Exotic Nuclei*; Cherepanov, E., Penionzhkevich, Y., Kamanin, D., Bark, R., Cornell, J., Eds.; World Scientific: Singapore, 2015; pp. 181–189. [CrossRef]
108. Ayyad, Y.; Bazin, D.; Beceiro-Novo, S.; Cortesi, M.; Mittig, W. Physics and technology of time projection chambers as active targets. *Eur. Phys. J. A* **2018**, *54*, 181. [CrossRef]
109. Bazin, D.; Ahn, T.; Ayyad, Y.; Beceiro-Novo, S.; Macchiavelli, A.O.; Mittig, W.; Randhawa, J.S. Low energy nuclear physics with active targets and time projection chambers. *Prog. Part. Nucl. Phys.* **2020**, *114*, 103790. [CrossRef]
110. Cortesi, M.; Pereira, J.; Bazin, D.; Ayyad, Y.; Cerizza, G.; Fox, R.; Zegers, R.G.T. Development of a novel MPGD-based drift chamber for the NSCL/FRIB S800 spectrometer. *JINST* **2020**, *15*, P03025. [CrossRef]
111. Blank, B.; Borge, M.J.G. Nuclear Structure at the Proton Drip Line: Advances with Nuclear Decay Studies. *Prog. Part. Nucl. Phys.* **2008**, *60*, 403–483. [CrossRef]
112. Hardy, J.C.; Towner, I.S. Superallowed $0^+ \rightarrow 0^+$ nuclear beta decays: 2020 critical survey, with implications for V_{ud} and CKM unitarity. *Phys. Rev. C* **2020**, *102*, 045501. [CrossRef]
113. Büscher, J.; Ponsaers, J.; Raabe, R.; Huyse, M.; Van Duppen, P.; Aksouh, F.; Smirnov, D.; Fynbo, H.O.U.; Hyldegaard, S.; Diget, C.A. β-Decay Studies with an Implantation Technique. *Nucl. Instrum. Methods Phys. Res. B* **2008**, *266*, 4652–4656. [CrossRef]
114. Hall, O.; Davinson, T.; Griffin, C.J.; Woods, P.J.; Appleton, C.; Bruno, C.G.; Estrade, A.; Kahl, D.; Sexton, L.; Burrows, I.; et al. The Advanced Implantation Detector Array (AIDA). *Nucl. Instrum. Methods Phys. Res. A* **2023**, *1050*, 168166. [CrossRef]
115. Lee, I.Y. The GAMMASPHERE. *Nucl. Phys. A* **1990**, *520*, 641c–655c. [CrossRef]
116. Muralithar, S.; Rani, K.; Kumar, R.; Singh, R.P.; Das, J.J.; Gehlot, J.; Golda, K.S.; Jhingan, A.; Madhavan, N.; Nath, S.; et al. Indian National Gamma Array at Inter University Accelerator Centre, New Delhi. *Nucl. Instrum. Methods Phys. Res. A* **2010**, *622*, 281–287. [CrossRef]
117. Lee, I.Y.; Clark, R.M.; Cromaz, M.; Deleplanque, M.A.; Descovich, M.; Diamond, R.M.; Fallon, P.; Macchiavelli, A.O.; Stephens, F.S.; Ward, D. GRETINA: A gamma ray energy tracking array. *Nucl. Phys. A* **2004**, *746*, 255–259. [CrossRef]
118. Paschalis, S.; Lee, I.Y.; Macchiavelli, A.O.; Campbell, C.M.; Cromaz, M.; Gros, S.; Pavan, J.; Qian, J.; Clark, R.M.; Crawford, H.L.; et al. The performance of the Gamma-Ray Energy Tracking In-beam Nuclear Array GRETINA. *Nucl. Instrum. Methods Phys. Res. A* **2013**, *709*, 44–55. [CrossRef]
119. Dewald, A.; Möller, O.; Petkov, P. Developing the Recoil Distance Doppler-Shift technique towards a versatile tool for lifetime measurements of excited nuclear states. *Prog. Part. Nucl. Phys.* **2012**, *67*, 786–839. [CrossRef]
120. Régis, J.-M.; Fraile, L.M.; Rudigier, M. γ–γ fast timing with high-performance LaBr$_3$(Ce) scintillators. *Prog. Part. Nucl. Phys.* **2025**, *141*, 104152. [CrossRef]
121. Tonev, D.; de Angelis, G.; Deloncle, I.; Goutev, N.; De Gregorio, G.; Pavlov, P.; Pantaleev, I.L.; Iliev, S.; Yavahchova, M.S.; Bizzeti, P.G.; et al. Transition probabilities in ^{31}P and ^{31}S: A test for isospin symmetry. *Phys. Lett. B* **2021**, *821*, 136603. [CrossRef]
122. Musolf, M.J.; Donnelly, T.W.; Dubach, J.; Pollock, S.J.; Kowalski, S.; Beise, E.J. Intermediate-energy semileptonic probes of the hadronic neutral current. *Phys. Rep.* **1994**, *239*, 1–178. [CrossRef]
123. Beck, D.H.; McKeown, R.D. Parity-violating electron scattering and nucleon structure. *Annu. Rev. Nucl. Part. Sci.* **2001**, *51*, 189–217. [CrossRef]
124. Kumar, K.S.; Mantry, S.; Marciano, W.J.; Souder, P.A. Low-energy measurements of the weak mixing angle. *Annu. Rev. Nucl. Part. Sci.* **2013**, *63*, 237–267. [CrossRef]
125. Abrahamyan, S.; Ahmed, Z.; Albataineh, H.; Aniol, K.; Armstrong, D.S.; Armstrong, W.; Averett, T.; Babineau, B.; Barbieri, A.; Bellini, V.; et al. Measurement of the Neutron Radius of ^{208}Pb through Parity Violation in Electron Scattering. *Phys. Rev. Lett.* **2012**, *108*, 112502. [CrossRef]
126. Adhikari, D.; Albataineh, H.; Androić, D.; Aniol, K.A.; Armstrong, D.S.; Averett, T.; Barcus, S.; Bellini, V.; Beminiwattha, R.S.; Benesch, J.F.; et al. Accurate determination of the neutron skin thickness of ^{208}Pb through parity-violation in electron scattering. *Phys. Rev. Lett.* **2021**, *126*, 172502. [CrossRef]
127. Adhikari, D.; Albataineh, H.; Androić, D.; Aniol, K.A.; Armstrong, D.S.; Averett, T.; Ayerbe Gayoso, C.; Barcus, S.K.; Bellini, V.; Beminiwattha, R.S.; et al. Precision determination of the neutral weak form factor of ^{48}Ca. *Phys. Rev. Lett.* **2022**, *129*, 042501. [CrossRef]

128. Androić, D.; Armstrong, D.S.; Asaturyan, A.; Averett, T.; Balewski, J.; Beaufait, J.; Beminiwattha, R.S.; Benesch, J.; Benmokhtar, F.; Birchall, J.; et al. First determination of the weak charge of the proton. *Phys. Rev. Lett.* **2013**, *111*, 141803. [CrossRef]
129. Yüksel, E.; Paar, N. Implications of Parity-Violating Electron Scattering Experiments on ^{48}Ca (CREX) and ^{208}Pb (PREX-II) for Nuclear Energy Density Functionals. *Phys. Lett. B* **2023**, *836*, 137622. [CrossRef]
130. Bosch, F.; Litvinov, Y.A.; Stöhlker, T. Nuclear physics with unstable ions at storage rings. *Prog. Part. Nucl. Phys.* **2013**, *73*, 84–140. [CrossRef]
131. Tu, X.L.; Wang, M.; Litvinov, Y.A.; Zhang, Y.H.; Xu, H.S.; Sun, Z.Y.; Audi, G.; Blaum, K.; Du, C.M.; Huang, W.X.; et al. Precision isochronous mass measurements at the storage ring CSRe in Lanzhou. *Nucl. Instrum. Methods Phys. Res. A* **2011**, *654*, 213–218. [CrossRef]
132. Litvinov, Y.A.; Bishop, S.; Blaum, K.; Bosch, F.; Brandau, C.; Chen, L.X.; Dillmann, I.; Egelhof, P.; Geissel, H.; Grisenti, R.E.; et al. Nuclear physics experiments with ion storage rings. *Nucl. Instrum. Methods Phys. Res. B* **2013**, *317*, 603–616. [CrossRef]
133. Steck, M.; Litvinov, Y.A. Heavy-ion storage rings and their use in precision experiments with highly charged ions. *Prog. Part. Nucl. Phys.* **2020**, *115*, 103811. [CrossRef]
134. Wang, M.; Zhang, M.; Zhou, X.; Zhang, Y.H.; Litvinov, Y.A.; Xu, H.S.; Chen, R.J.; Deng, H.Y.; Fu, C.Y.; Ge, W.W.; et al. $B\rho$-defined isochronous mass spectrometry: An approach for high-precision mass measurements of short-lived nuclei. *Phys. Rev. C* **2022**, *106*, L051301. [CrossRef]
135. Alder, K.; Winther, A. *Electromagnetic Excitation: Theory of Coulomb Excitation with Heavy Ions*; North-Holland: Amsterdam, The Netherlands, 1975.
136. Gade, A.; Glasmacher, T. In-beam nuclear spectroscopy of bound states with fast exotic ion beams. *Prog. Part. Nucl. Phys.* **2008**, *60*, 161–224. [CrossRef]
137. Blaich, T.; Elze, T.W.; Emling, H.; Freiesleben, H.; Grimm, K.; Henning, W.; Holzmann, R.; Ickert, G.; Keller, J.G.; Klingler, H.; et al. A large area detector for high-energy neutrons (LAND). *Nucl. Instrum. Methods Phys. Res. A* **1992**, *314*, 136–154. [CrossRef]
138. Nakamura, T.; Kondo, Y. Large acceptance spectrometers for invariant mass spectroscopy of exotic nuclei and future developments. *Nucl. Instrum. Methods Phys. Res. B* **2016**, *376*, 156–161. [CrossRef]
139. Luther, B.; Baumann, T.; Thoennessen, M.; Brown, J.; DeYoung, P.; Finck, J.; Hinnefeld, J.; Howes, R.; Kemper, K.; Pancella, P.; et al. MoNA—The Modular Neutron Array. *Nucl. Instrum. Methods Phys. Res. A* **2003**, *505*, 33–35. [CrossRef]
140. Baumann, T.; Brown, J.A.; DeYoung, P.; Finck, J.E.; Hinnefeld, J.D.; Howes, R.; Kemper, K.W.; Luther, B.A.; Pancella, P.V.; Peaslee, G.F.; et al. MoNA—The Modular Neutron Array at the NSCL. *AIP Conf. Proc.* **2003**, *680*, 554–556. [CrossRef]
141. Lunney, D.; Pearson, J.M.; Thibault, C. Recent Trends in the Determination of Nuclear Masses. *Rev. Mod. Phys.* **2003**, *75*, 1021–1082. [CrossRef]
142. Kluge, H.-J. Penning trap mass spectrometry of radionuclides. *Int. J. Mass Spectrom.* **2013**, *349–350*, 26–37. [CrossRef]
143. Boehnlein, A.; Diefenthaler, M.; Sato, N.; Schram, M.; Ziegler, V.; Fanelli, C.; Hjorth-Jensen, M.; Horn, T.; Kuchera, M.P.; Lee, D.; et al. Colloquium: Machine learning in nuclear physics. *Rev. Mod. Phys.* **2022**, *94*, 031003. [CrossRef]
144. Liu, Z.W.; Qian, Z.; Xing, R.Y.; Niu, J.R.; Sun, B.Y. Nuclear fourth-order symmetry energy and its effects on neutron star properties in the relativistic Hartree-Fock theory. *Phys. Rev. C* **2018**, *97*, 025801. [CrossRef]
145. Somasundaram, R.; Drischler, C.; Tews, I.; Margueron, J. Constraints on the nuclear symmetry energy from asymmetric-matter calculations. *Phys. Rev. C* **2021**, *103*, 045803. [CrossRef]
146. Senger, P. Probing the Equation of State of Dense Nuclear Matter by Heavy Ion Collision Experiments. *Symmetry* **2024**, *16*, 1162. [CrossRef]
147. Typel, S.; Brown, B.A. Neutron radii and the neutron equation of state in relativistic models. *Phys. Rev. C* **2001**, *64*, 027302. [CrossRef]
148. Chen, L.-W.; Ko, C.M.; Li, B.-A. Nuclear matter symmetry energy and the neutron skin thickness of heavy nuclei. *Phys. Rev. C* **2005**, *72*, 064309. [CrossRef]
149. Reinhard, P.-G.; Nazarewicz, W. Information Content of a New Observable: The Case of the Nuclear Neutron Skin. *Phys. Rev. C* **2010**, *81*, 051303(R). [CrossRef]
150. Tamii, A.; Poltoratska, I.; von Neumann-Cosel, P.; Fujita, Y.; Adachi, T.; Bertulani, C.A.; Carter, J.; Dozono, M.; Fujita, H.; Fujita, K.; et al. Complete Electric Dipole Response and the Neutron Skin in ^{208}Pb. *Phys. Rev. Lett.* **2011**, *107*, 062502. [CrossRef]
151. Piekarewicz, J.; Agrawal, B.K.; Colò, G.; Nazarewicz, W.; Paar, N.; Reinhard, P.-G.; Roca-Maza, X.; Vretenar, D. Electric Dipole Polarizability and the Neutron Skin. *Phys. Rev. C* **2012**, *85*, 041302(R). [CrossRef]
152. Savran, D.; Aumann, T.; Zilges, A. Experimental Studies of the Pygmy Dipole Resonance. *Prog. Part. Nucl. Phys.* **2013**, *70*, 210–245. [CrossRef]
153. Piekarewicz, J. Pygmy Dipole Resonance as a Constraint on the Neutron Skin of Heavy Nuclei. *Phys. Rev. C* **2006**, *73*, 044325. [CrossRef]
154. Demorest, P.B.; Pennucci, T.; Ransom, S.M.; Roberts, M.S.E.; Hessels, J.W.T. A two-solar-mass neutron star measured using Shapiro delay. *Nature* **2010**, *467*, 1081–1083. [CrossRef] [PubMed]

155. Antoniadis, J.; Freire, P.C.C.; Wex, N.; Tauris, T.M.; Lynch, R.S.; van Kerkwijk, M.H.; Kramer, M.; Bassa, C.; Dhillon, V.S.; Driebe, T.; et al. A massive pulsar in a compact relativistic binary. *Science* **2013**, *340*, 448. [CrossRef] [PubMed]
156. Roberts, B.M.; Dzuba, V.A.; Flambaum, V.V. Parity and time-reversal violation in atomic systems. *Annu. Rev. Nucl. Part. Sci.* **2015**, *65*, 63–86. [CrossRef]
157. Engel, J.; Menéndez, J. Status and future of nuclear matrix elements for neutrinoless double-beta decay: A review. *Rep. Prog. Phys.* **2017**, *80*, 046301. [CrossRef]
158. Abel, C.; Afach, S.; Ayres, N.J.; Baker, C.A.; Ban, G.; Bison, G.; Bodek, K.; Bondar, V.; Burghoff, M.; Chanel, E.; et al. Measurement of the permanent electric dipole moment of the neutron. *Phys. Rev. Lett.* **2020**, *124*, 081803. [CrossRef]
159. Spevak, V.; Auerbach, N.; Flambaum, V.V. Enhanced T-odd, P-odd electromagnetic moments in reflection asymmetric nuclei. *Phys. Rev. C* **1997**, *56*, 1357–1369. [CrossRef]
160. Dobaczewski, J.; Engel, J. Nuclear time-reversal violation and the Schiff moment of ^{225}Ra. *Phys. Rev. Lett.* **2005**, *94*, 232502. [CrossRef] [PubMed]
161. Butler, P.A.; Nazarewicz, W. Intrinsic reflection asymmetry in atomic nuclei. *Rev. Mod. Phys.* **1996**, *68*, 349–421. [CrossRef]
162. Dobaczewski, J.; Engel, J.; Kortelainen, M.; Becker, P. Correlating Schiff moments in the light actinides with octupole moments. *Phys. Rev. Lett.* **2018**, *121*, 232501. [CrossRef]
163. Parker, R.H.; Dietrich, M.R.; Kalita, M.R.; Lemke, N.D.; Bailey, K.G.; Bishof, M.N.; Greene, J.P.; Holt, R.J.; Korsch, W.; Lu, Z.-T.; et al. First measurement of the atomic electric dipole moment of ^{225}Ra. *Phys. Rev. Lett.* **2015**, *114*, 233002. [CrossRef] [PubMed]
164. Flambaum, V.V.; DeMille, D.; Kozlov, M.G. Time-reversal symmetry violation in molecules induced by nuclear magnetic quadrupole moments. *Phys. Rev. Lett.* **2014**, *113*, 103003. [CrossRef]
165. Schechter, J.; Valle, J.W.F. Neutrinoless double-β decay in SU(2)$\times$U(1) theories. *Phys. Rev. D* **1982**, *25*, 2951–2954. [CrossRef]
166. Dolinski, M.J.; Poon, A.W.P.; Rodejohann, W. Neutrinoless double-beta decay: Status and prospects. *Annu. Rev. Nucl. Part. Sci.* **2019**, *69*, 219–251. [CrossRef]
167. Gómez-Cadenas, J.J.; Martín-Albo, J.; Menéndez, J.; Mezzetto, M.; Monrabal, F.; Sorel, M. The search for neutrinoless double-beta decay. *Riv. Nuovo Cimento* **2023**, *46*, 619–692. [CrossRef]
168. Gando, A. on behalf of the KamLAND-Zen Collaboration. KamLAND-Zen 800. *Proc. Sci.* **2022**, *414*, 583. [CrossRef]
169. Burlac, N.; LEGEND Collaboration. Early results of the LEGEND-200 experiment. *Nucl. Instrum. Methods Phys. Res. A* **2025**, *1080*, 170779. [CrossRef]
170. Adhikari, G.; Al Kharusi, S.; Angelico, E.; Anton, G.; Arnquist, I.J.; Badhrees, I.; Bane, J.; Belov, V.; Bernard, E.P.; Bhatta, T.; et al. nEXO: Neutrinoless Double Beta Decay Search Beyond 10^{28} Year Half-Life Sensitivity. *J. Phys. G Nucl. Part. Phys.* **2022**, *49*, 015104. [CrossRef]
171. Abgrall, N.; Abt, I.; Agostini, M.; Alexander, A.; Andreoiu, C.; Araujo, G.R.; Avignone, F.T., III; Bae, W.; Bakalyarov, A.; Balata, M.; et al. LEGEND-1000 Preconceptual Design Report. *arXiv* **2021**, arXiv:2107.11462. [CrossRef]
172. Cappuzzello, F.; Agodi, C.; Cavallaro, M.; Carbone, D.; Tudisco, S.; Lo Presti, D.; Oliveira, J.R.B.; Finocchiaro, P.; Colonna, M.; Rifuggiato, D.; et al. The NUMEN project: NUclear Matrix Elements for Neutrinoless double beta decay. *Eur. Phys. J. A* **2018**, *54*, 72. [CrossRef]
173. Ahmadi, M.; Alves, B.X.R.; Baker, C.J.; Bertsche, W.; Butler, E.; Capra, A.; Carruth, C.; Cesar, C.L.; Charlton, M.; Cohen, S.; et al. Observation of the hyperfine spectrum of antihydrogen. *Nature* **2017**, *548*, 66–69. [CrossRef] [PubMed]
174. Ahmadi, M.; Alves, B.X.R.; Baker, C.J.; Bertsche, W.; Capra, A.; Carruth, C.; Cesar, C.L.; Charlton, M.; Cohen, S.; Collister, R.; et al. Characterization of the 1S–2S transition in antihydrogen. *Nature* **2018**, *557*, 71–75. [CrossRef]
175. Ulmer, S.; Smorra, C.; Mooser, A.; Franke, K.; Nagahama, H.; Schneider, G.; Higuchi, T.; Van Gorp, S.; Blaum, K.; Matsuda, Y.; et al. High-precision comparison of the antiproton-to-proton charge-to-mass ratio. *Nature* **2015**, *524*, 196–199. [CrossRef]
176. Smorra, C.; Sellner, S.; Borchert, M.J.; Harrington, J.A.; Higuchi, T.; Nagahama, H.; Tanaka, T.; Mooser, A.; Schneider, G.; Bohman, M.; et al. A parts-per-billion measurement of the antiproton magnetic moment. *Nature* **2017**, *550*, 371–374. [CrossRef] [PubMed]
177. Andreev, V.; Ang, D.G.; DeMille, D.; Doyle, J.M.; Gabrielse, G.; Haefner, J.; Hutzler, N.R.; Lasner, Z.; Meisenhelder, C.; O'Leary, B.R.; et al. Improved limit on the electric dipole moment of the electron. *Nature* **2018**, *562*, 355–360. [CrossRef]
178. Cairncross, W.B.; Gresh, D.N.; Grau, M.; Cossel, K.C.; Roussy, T.S.; Ni, Y.; Zhou, Y.; Ye, J.; Cornell, E.A. Precision measurement of the electron's electric dipole moment using trapped molecular ions. *Phys. Rev. Lett.* **2017**, *119*, 153001. [CrossRef]
179. Isaev, T.A.; Hoekstra, S.; Berger, R. Laser-cooled RaF as a promising candidate to measure molecular parity violation. *Phys. Rev. A* **2010**, *82*, 052521. [CrossRef]
180. Isaev, T.A.; Berger, R. Polyatomic Candidates for Cooling of Molecules with Lasers from Simple Theoretical Concepts. *Phys. Rev. Lett.* **2016**, *116*, 063006. [CrossRef] [PubMed]